Title

Dentate gyrus and CA3 GABAergic interneurons bidirectionally modulate signatures of internal and external drive to CA1

Journal

Cell Reports, 37(13)

ISSN

2639-1856

Authors

Aery Jones, Emily A

Rao, Antara

Zilberter, Misha

et al.

Publication Date

2021-12-01

DOI

10.1016/j.celrep.2021.110159

Peer reviewed

HHS Public Access

Author manuscript

Cell Rep. Author manuscript; available in PMC 2022 May 05.

Published in final edited form as:

Cell Rep. 2021 December 28; 37(13): 110159. doi:10.1016/j.celrep.2021.110159.

Dentate Gyrus and CA3 GABAergic Interneurons Bidirectionally Modulate Signatures of Internal and External Drive to CA1

Emily A. Aery Jones[1,2], **Antara Rao**[1,3], **Misha Zilberter**[1], **Biljana Djukic**[1], **Jason S. Bant**[1], **Anna K. Gillespie**[4], **Nicole Koutsodendris**[1,3], **Maxine Nelson**[1,2], **Seo Yeon Yoon**[1], **Ky Huang**[1], **Heidi Yuan**[1], **Theodore M. Gill**[1], **Yadong Huang**[1,2,3,5,6,*], **Loren M. Frank**[4,7,8,*]

[1]Gladstone Institute of Neurological Disease, San Francisco, CA 94158, USA.

[2]Biomedical Sciences Graduate Program, University of California, San Francisco, CA 94143, USA

[3]Developmental & Stem Cell Biology Graduate Program, University of California, San Francisco, CA 94143, USA

[4]Kavli Institute for Fundamental Neuroscience and Department of Physiology, University of California, San Francisco, CA 94143, USA

[5]Departments of Neurology and Pathology, University of California, San Francisco, CA 94143, USA

[6]Gladstone Center for Translational Advancement, San Francisco, CA 94158, USA

[7]Howard Hughes Medical Institute, Chevy Chase, MD 20815, USA

[8]Lead contact

SUMMARY

Specific classes of GABAergic neurons play specific roles in regulating information processing in the brain. In the hippocampus, two major classes – parvalbumin-expressing (PV^+) and somatostatin-expressing (SST^+) – differentially regulate endogenous firing patterns and target subcellular compartments of principal cells. How these classes regulate the flow of information throughout the hippocampus is poorly understood. We hypothesize that PV^+ and SST^+ interneurons in the dentate gyrus (DG) and CA3 differentially modulate CA3 patterns of output, thereby altering the influence of CA3 on CA1. We find that while suppressing either interneuron

[*]**Correspondence should be addressed to:** Loren Frank (loren.frank@uscf.edu) or Yadong Huang (yadong.huang@gladstone.ucsf.edu).

AUTHOR CONTRIBUTIONS

E.A.A.J., Y.H., and L.M.F. designed and coordinated the study. E.A.A.J. carried out most studies, performed all data analysis, and created all figures. E.A.A.J. and L.M.F wrote the manuscript. A.R., A.K.G., and J.S.B. assisted with *in vivo* electrophysiological recordings. M.Z. and B.D. performed *ex vivo* electrophysiology experiments. A.R., N.K., M.N., and H.Y. assisted with immunohistochemistry. S.Y.Y. managed mouse lines and performed perfusions. K.H. and T.M.G. assisted with behavioral task design and provided advice on data analysis. Y.H. and L.M.F. provided advice on data analysis and interpretations, edited the manuscript, and supervised the project.

DECLARATION OF INTERESTS

Y.H. is a co-founder and scientific advisory board member of E-Scape Bio, Inc., GABAeron, Inc., and Mederon Bio, LLC. Other authors declare no competing financial interests.

INCLUSION AND DIVERSITY

We worked to ensure sex balance in the selection of non-human subjects. While citing references scientifically relevant for this work, we also actively worked to promote gender balance in our reference list.

class increases DG and CA3 output, the effects on CA1 were very different. Suppressing PV^+ interneurons increases local field potential signatures of coupling from CA3 to CA1 and decreases signatures of coupling from entorhinal cortex to CA1; suppressing SST^+ interneurons has the opposite effect. Thus, DG and CA3 PV^+ and SST^+ interneurons bidirectionally modulate the flow of information through the hippocampal circuit.

eTOC Blurb

Aery Jones et al. examine how two major inhibitory interneuron classes in regions upstream of hippocampal area CA1 gate internal hippocampal versus external entorhinal inputs to CA1. They find opposing effects of the two classes on interval versus external drive to CA1.

Graphical Abstract

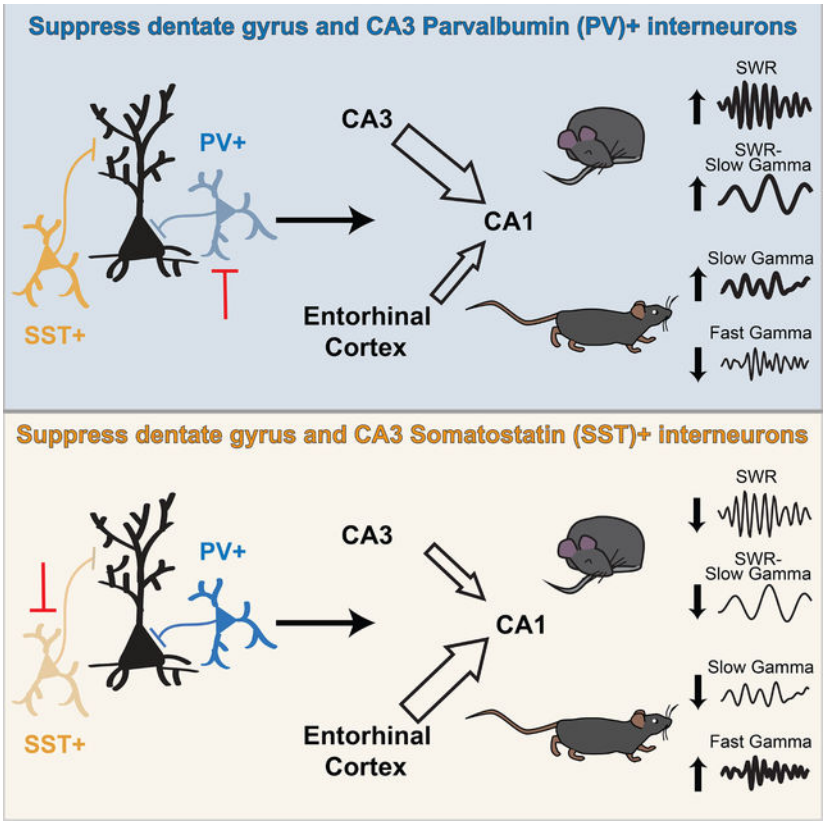

INTRODUCTION

GABAergic interneurons regulate principal cell input and output and act as hubs for controlling network activity throughout the brain (McKenzie, 2017). These interneurons are highly heterogeneous (Klausberger and Somogyi, 2008), and distinct classes may play distinct roles in balancing internal and external input drive to local circuits.

In the hippocampus, a brain structure critical for encoding, consolidation, and retrieval of memories, the majority of GABAergic interneurons are either parvalbumin-expressing

(PV^+) or somatostatin-expressing (SST^+) (Jinno and Kosaka, 2002, 2003). PV^+ and SST^+ interneurons throughout the hippocampus are distinguished by their subcellular spatial domains, firing properties, pyramidal cell spike modulation mechanisms, and temporal coordination (Klausberger and Somogyi, 2008). These two interneuron classes are well characterized in CA1, where they are uniquely positioned to bidirectionally regulate information flow from the two major inputs: internal input from CA3 and external input from entorhinal cortex (EC). PV^+ interneurons mainly target somatic and perisomatic compartments and thus regulate principal cell excitability and precise spike timing (Klausberger and Somogyi, 2008; Lovett-Barron et al., 2012; Miles et al., 1996; Royer et al., 2012). In CA1, these cells are preferentially recruited by excitatory EC inputs and are thus the main drivers of feedforward inhibition (Freund and Buzsáki, 1996; Gulyás et al., 1999; Lee et al., 2016; Wheeler et al., 2015). In contrast, SST^+ interneurons mainly target distal apical dendrites – which receive extrahippocampal excitatory inputs from the EC and medial septum (MS) – and gate the influence of those pathways, thereby affecting the magnitude of principal cell spiking (Blasco-Ibáñez and Freund, 1995; Klausberger and Somogyi, 2008; Lovett-Barron et al., 2012; Sik et al., 1995, 1997; Takács et al., 2012). These cells receive primarily local inputs from pyramidal cells and thus provide feedback inhibition (Freund and Buzsáki, 1996; Wheeler et al., 2015). Consistent with these patterns of inputs, potentiation of PV^+ interneurons attenuates CA3 inputs while potentiation of CA1 SST^+ interneurons attenuates EC inputs (Fernández-Ruiz et al., 2017; Udakis et al., 2020).

Whether PV^+ and SST^+ interneurons in the upstream regions of the dentate gyrus (DG) and CA3 play similar distinct roles is unknown. Since both populations are inhibitory, we would expect that suppressing either PV^+ or SST^+ interneurons in DG and CA3 would lead to greater total spiking output from CA3 and thus greater input to CA1. Moreover, there is some overlap between PV and SST expression (Jinno and Kosaka, 2000), making it unclear whether broadly manipulating these genetically-defined cell classes would modulate outputs in opposing directions.

However, given their similarities to analogous populations in CA1 (Klausberger and Somogyi, 2008), DG and CA3 PV^+ interneurons would be expected to provide feed-forward inhibition at the soma, thus suppressing internal DG to CA3 and CA3 to CA3 inputs. Conversely, as DG and CA3 SST^+ interneurons are thought to provide feedback inhibition at the level of EC inputs, we would expect them to suppress those external inputs. Thus, suppressing DG and CA3 PV^+ interneurons might ungate internal drive in DG and CA3, while suppressing DG and CA3 SST^+ interneurons might ungate external drive. If the resulting patterns of CA3 activity differentially engage CA1, we would predict that suppressing either PV^+ or SST^+ interneurons in DG and CA3 would enhance DG and CA3 spiking outputs, but this increase in output could have different effects on CA1.

To measure these potential effects, we took advantage of known signatures of information flow in the hippocampal network. During immobility, high CA3 drive to CA1 is associated with sharp-wave ripple (SWR) events (Buzsáki et al., 1992; Csicsvari et al., 2000; Ylinen et al., 1995) that can be detected as increases in ripple frequency (125–200 Hz) power in CA1. blocking CA3 input to CA1 reduces SWR rate, slows SWR frequency, and increases multi-unit activity (MUA) recruitment to SWRs (Middleton and McHugh, 2016; Nakashiba

et al., 2009; Yamamoto and Tonegawa, 2017) while increasing CA3 drive to CA1 increases SWR rate, SWR frequency, SWR-coincident slow gamma (SG) power, and sharp wave (SW) amplitude (Ramirez-Villegas et al., 2018; Wu et al., 2015). By contrast, blocking direct EC input to CA1 diminishes SWR chains, but has no other observable effects on SWR rate, frequency, or duration (Yamamoto and Tonegawa, 2017), while lesioning EC increases SWR rate (Bragin et al., 1995a). Thus, SWR properties provide information about CA3 and EC drive to CA1, and these signatures are bidirectional: decreased internal CA3 drive is associated with decreased SWR activity, and decreased external EC drive is associated with increased SWR activity.

During movement, EC drive to CA1 is associated with fast gamma (FG; 50–100 Hz) oscillations, while CA3 drive to CA1 is associated with SG (20–50 Hz) oscillations (Bragin et al., 1995b; Colgin, 2016; Colgin et al., 2009). Blocking synaptic inputs from CA3 to CA1 impacts CA1 SG power and modulation by theta phase while not detectably affecting CA1 SG frequency and coherence across regions (Middleton and McHugh, 2016). Direct EC layer III inputs to CA1 have been shown to contribute to CA1 FG activity (Yamamoto et al., 2014). However, lesioning inputs from CA3 to CA1 also reduces CA1 FG power, suggesting that FG reflects both inputs (Middleton and McHugh, 2016). SG and FG are in turn organized by theta (5–11 Hz), which is partly driven by EC excitatory inputs to CA1 (Colgin, 2015). Theta is not detectably disrupted by blocking CA3 inputs to CA1 (Middleton and McHugh, 2016) but does diminish in power and frequency throughout the hippocampus when EC is lesioned (Bragin et al., 1995b; Buzsáki et al., 1983; Maurer et al., 2006; Ormond et al., 2015; Schlesiger et al., 2015). Thus, theta and gamma rhythms during movement can provide information about internal CA3 and external EC drive to CA1.

We therefore asked whether modulation of specific interneuron types in DG and CA3 could alter these signatures of EC and CA3 drive to CA1. We found that while suppression of either interneuron type led to an increase in DG and CA3 spiking output, suppressing PV^+ interneurons increased signatures of CA3 coupling to CA1 and decreased those of EC coupling to CA1, while suppressing SST^+ interneurons decreased signatures of CA3 coupling to CA1 and increased those of EC coupling to CA1. Our findings indicate that PV^+ and SST^+ interneurons in DG and CA3 can bidirectionally alter patterns of activity in DG and CA3, altering the balance of LFP signatures of EC and CA3 drive in CA1.

RESULTS

Recording *in vivo* hippocampal LFP during chemogenetic suppression of PV^+ and SST^+ interneurons in DG and CA3

We used a Cre-dependent chemogenetic approach to silence specific interneuron classes in DG and CA3. We bilaterally injected PV-Cre, SST-Cre, and PV-Cre/SST-Cre mice with AAV5-hSyn-DIO-hM4D(Gi)-mCherry or with AAV5-hSyn-DIO-mCherry into the DG hilus, and then implanted a 32-site silicon electrode array into the right dorsal hippocampus (Figure 1A–C). HM4D expression was highly co-localized with PV and SST expression (Figure S1A–C and Table S1) and extended throughout DG and CA3 from dorsal to ventral hippocampus, with no expression in CA1 or CA2 (Figure 1D). We confirmed hM4D function in *ex vivo* brain slices by observing that clozapine N-oxide (CNO) application

reduced firing rates in PV^+ and SST^+ interneurons expressing hM4D (Figure S1D), hyperpolarized resting membrane potentials by 8.6 ± 1.3mV (Figure S1E), and decreased input resistance by 31.3 ± 9.9 MΩ (Figure S1F). After viral expression, we recorded LFP activity from CA1, CA3, and DG over 6 daily sessions, alternating CNO and vehicle treatment across days (Figure 1A). CNO was used to suppress interneuron activity for the duration of the each recording. We collected data from three cohorts of animals: the first and second underwent only home cage recordings, and the third underwent linear track recordings followed by home cage recordings.

We assessed LFP features as a readout for changes in internal CA3 versus external EC drive to CA1, focusing on features previously identified to be modulated by CA3 or EC drive. We took advantage of a statistical approach known as a Linear Mixed Model (LMM) to assess differences between groups (genotype effect) while accounting for variability both within and across individuals. We evaluated differences between significant treatment effects (genotype-treatment interaction effect) to determine which effects were significantly different between genotypes (referred to as specific). We further sought to control our false positive rate and so only report findings which survive Holm-Bonferroni correction across all comparisons in each experiment (see Methods). Therefore, comparisons are only interpreted as significant if their Holm-Bonferroni corrected p values fall below $\alpha = 0.05$.

Suppressing PV^+ or SST^+ interneurons bidirectionally modulates SWR signatures of CA3 coupling to CA1

We first asked whether PV^+ or SST^+ interneurons in DG and CA3 modulate signatures of CA3 coupling to CA1 as measured through increased SWR activity during immobility (<1 cm/s for ≥30 s) in 1-hour daily home cage sessions (Figure 2A and 3A). We hypothesized that suppressing DG and CA3 PV^+ interneurons might ungate internal DG and CA3 inputs and thus changing DG and CA3 firing patterns in a manner that facilitates internally driven patterns of activity (e.g. SWRs) in CA1. Conversely, suppressing DG and CA3 SST^+ interneurons might ungate EC inputs and perhaps change DG and CA3 firing patterns in a manner that increases CA1 receptivity to EC drive.

We began by measuring the effect of interneuron suppression on CA3 input to CA1, starting with a first cohort of mice implanted with a single-shank electrode with 50 μm site spacing to enable current source density (CSD) analysis (Figure 2A–B). During SWRs, CSD sources and sinks in stratum radiatum – the layer of CA3 input – increased when either PV^+ or SST^+ interneurons were suppressed (Figure 2C–F). Furthermore, in a second cohort of mice implanted with a four-shank electrode to enable recordings from all hippocampal subregions, we found that suppressing either class increased the extent to which DG and CA3, but not CA1, MUA increased during SWRs (Figure 3B). Thus, CA3 input to CA1 increased regardless of which interneuron class was suppressed.

As SWRs depend on CA3 input to CA1, one might predict that SWR events themselves would be more prevalent following suppression of both PV^+ and SST^+ interneurons. This was not the case. Instead, we found evidence for opposing patterns of modulation. Suppressing PV^+ interneurons increased SWR rate while suppressing SST^+ interneurons decreased SWR rate, and these effects were significantly different between genotypes

(Figure 3C). This effect was not due to differences in SWR detection or baseline MUA (Table S2). There was also a decrease in the proportion of SWRs that participated in chains (Figure 3D) in both genotypes, indicating that broadly increasing DG and CA3 output influences chaining of SWRs. Finally, we examined fast ripples (Valero et al., 2017) to determine whether the observed changes in SWR rate were due to epileptic activity, as ablation or silencing of CA1 or subiculum interneurons can lead to seizures (Drexel et al., 2017; Spampanato and Dudek, 2017). While we observed no behavioral seizures, we did detect a modest increase in the incidence of rare fast ripples when PV^+ interneurons were suppressed (Table S2), indicating that increased CA3 drive might increase potentially pathological SWRs.

We then assessed the structure of these SWRs and found further evidence for interneuron subtype-specific effects. SST^+ interneuron suppression increased SWR length, an effect not seen following PV^+ interneuron suppression (Figure 3E). Since EC activity can increase prior to SWRs longer than 100 ms (Oliva et al., 2018), we also looked specifically at the proportion of SWRs longer than 100 ms and found an increase when SST^+ interneurons were suppressed (% of SWRs > 100 ms: vehicle 38.5% vs CNO 49.6%, paired t test, $t(15) = 3.67$, $p = 0.002$). Thus, suppressing DG and CA3 SST^+ interneurons has effects consistent with facilitated EC input to CA1.

Similar differences were seen for other SWR parameters. PV^+, but not SST^+, interneuron suppression increased the instantaneous frequency of SWRs (Figure 3F) and sharp-wave (SW) amplitude in CA1 (Figure 3G). However, SWR size was smaller when PV^+ interneurons were suppressed (Figure S2A) despite no change in CA1 MUA recruitment. Overall, suppressing PV^+ interneurons increased SWR signatures of CA3 drive to CA1, while suppressing SST^+ interneurons decreased these signatures, consistent with opposing roles in regulating drive to CA1.

Suppressing PV^+ or SST^+ interneurons bidirectionally modulates SWR-coincident SG signatures of CA3 coupling to CA1

Next, we measured SG power coincident with ripples, which is driven by CA3 (Carr et al., 2012; Gillespie et al., 2016; Ramirez-Villegas et al., 2015, 2018). Based on the results above, we again hypothesized that suppressing PV^+ interneurons would have similar effects to increasing CA3 drive to CA1, while suppressing SST^+ interneurons would have similar effects to increasing EC drive to CA1.

Following suppression of PV^+ interneurons, SG power in CA1 was higher across all rest during CNO epochs (Figure 4A) – consistent with increased CA3 drive (Kemere et al., 2013) – and had higher variance in all 3 subregions (Table S3). We therefore used the mean and SD of SG power calculated from vehicle-treated epochs to z-score SG power during all epochs. Suppressing PV^+ interneurons led to greater SWR-coincident SG power in CA1, CA3, and DG (Figure 4A, 3B, 3D, and S3B). Interestingly, the extent of CA1 SWR-coincident SG power increase correlated across animals with the extent of SW amplitude increase and the extent of SWR frequency increase (Figure S3C–D), suggesting these features reflect similar underlying mechanisms, as has been suggested previously (Oliva et al., 2018; Stark et al., 2014). These effects were specific to PV^+ interneurons, as

suppressing SST^+ interneurons did not change SG power either at baseline (Table S2) or during SWRs (Figure 4A, 4C, 4D, and S2B). Similarly, only PV^+ suppression enhanced the increase in SG coherence between CA1 and CA3 or DG during SWRs, (Figure 4E). This was not merely due to increases in activity, as CA1 MUA did not increase (Figure 3B). Overall, suppressing PV^+ interneurons increased SWR activity, consistent with a facilitation of internally generated CA3 spiking patterns that lead to SWRs, while suppressing SST^+ interneurons decreased SWR activity, consistent with a role in ungating EC inputs to DG and CA3 and thereby changing DG and CA3 firing patterns in a manner that suppressed SWR activity.

Suppressing PV^+ or SST^+ interneurons modulate local CA3 SWRs and DG spikes

We further examined how DG and CA3 interneurons affect local oscillations during rest, specifically CA3 SWRs and dentate spikes (DS) (Figure S3A). As expected, only a subset of CA3 SWRs overlapped in time with CA1 SWRs (37.18%, averaged over all PV-Cre and SST-Cre vehicle sessions), presumably reflecting the potential for SWRs to be generated across the extent of Cornus Ammonis. Nonetheless, we observed that, similar to MUA during CA1 SWRs, suppressing either interneuron class increased the extent to which CA3 MUA increased during CA3 SWRs (Figure S3B).

As SWRs are generated by a rapid increase in activity in CA3 (Csicsvari et al., 2000), one might predict that CA3 SWRs would be more prevalent following suppressing of either PV^+ or SST^+ interneurons. Instead, as for CA1 SWRs, suppressing PV^+ and SST^+ interneurons distinctly modulated SWR properties. Suppressing PV^+ interneurons decreased CA3 SWR rate, while suppressing SST^+ interneurons increased CA3 SWR rate (Figure S3C). This effect was not due to differences in CA3 SWR detection or baseline MUA (Table S2). Suppression of either interneuron type increased CA3 SWR length (Figure S3D). Finally, PV^+ interneuron suppression decreased CA3 SWR instantaneous frequency (Figure S3E). We note that the changes in CA3 SWR properties (rates, length, and instantaneous frequencies) seen during PV^+ interneuron suppression were opposite in sign to those seen when CA1 SWRs were examined, indicating that modulation of CA1 SWRs was not simply a downstream readout of modulation of CA3 SWRs.

We then examined DS, which are driven by EC input to DG (Bragin et al., 1995a). MUA during DS is largely driven by inhibitory neurons (Penttonen et al., 1997), thus we hypothesized that suppressing either interneuron class might decrease DG MUA during DS. Instead, DS MUA did not change (Figure S3F), suggesting that other inhibitory neurons may have been disinhibited by this suppression. Suppression of either PV^+ or SST^+ interneurons decreased DS rate (Figure S3G), suggesting that both interneuron classes might contribute to the synchronized inhibition observed during DS (Penttonen et al., 1997). Suppressing PV^+ interneurons also increased DS length while decreasing DS amplitude, while suppressing SST^+ interneurons had no detectable effect on these features.

Suppressing PV+ or SST+ interneurons bidirectionally modulates SG signatures of CA3 coupling to CA1 during movement

We next asked whether these bidirectional effects extended to LFP features observed during movement. We examined CA1 SG, FG, and theta activity during movement (>1 cm/s) in daily 30-minute linear track sessions, focusing on stratum pyramidale (Figure 5A), though similar results were found in recordings from strata radiatum (where CA3 inputs terminate) and lacunosum moleculare (where EC inputs terminate; data not shown). We asked whether suppressing DG and CA3 PV^+ interneurons ungates internally driven CA3 activity patterns, while suppressing DG and CA3 SST^+ interneurons ungates EC inputs and thus change firing patterns in a manner consistent with increased effective EC drive to CA1.

We again began by measuring the effect of interneuron suppression on spiking output and found that suppressing either class increased MUA during movement in DG and CA3, but not CA1 (Figure 5B). Thus, just as for SWR-related activity, suppressing interneurons unidirectionally disinhibited local DG and CA3 cells while leaving CA1 spiking rates intact.

Despite this, PV^+ and SST^+ interneurons differentially modulated SG during movement. Suppressing PV^+ interneurons in DG and CA3 amplified SG power in CA1, but there was no detectable effect following suppression of SST^+ interneurons. By contrast, suppressing PV^+ interneurons had no detectable effect on SG power in DG and CA3, while suppressing SST^+ interneurons dampened SG power locally in DG and CA3. All these effects were significantly different across genotypes (Figure 5C–D and S4A). Relatedly, suppressing PV^+ interneurons enhanced SG coherence between CA1 and CA3 (Figure 5E). Thus, like during rest periods, suppressing PV^+ interneurons increased the amplitude of SG in CA1 and the coherence of SG, across regions, consistent with an increase of CA3 drive to CA1. In addition, suppressing PV^+ interneurons, but not SST^+ interneurons, reduced SG frequency throughout the hippocampus (Figure 5F and S4B). Finally, suppressing PV^+ interneurons increased theta modulation of SG only locally in DG and CA3, while suppressing SST^+ interneurons reduced theta modulation of SG in CA1, and these effects were again detectably different between genotypes. Overall, suppressing PV^+ interneurons amplified SG while suppressing SST^+ interneurons had the opposite or no effect.

Suppressing PV+ or SST+ interneurons bidirectionally modulates FG signatures of EC coupling to CA1 during movement

The results above indicate that suppressing PV^+ or SST^+ interneurons in DG and CA3 can lead to quite different effects in CA1, despite the shared increase in DG and CA3 multiunit activity. As described above, this suggests that the two interneuron classes differentially effect the organization of activity transmitted from CA3 to CA1, and thereby have different effects on CA1. If so, then suppressing SST^+ interneurons in DG and CA3 would also enhance FG in CA1, despite this typically being characterized as a signature of direct EC input to CA1 (Colgin, 2016). Further, if this hypothesis is correct, then suppressing PV^+ interneurons in DG and CA3 would have the opposite or no effect, as this would facilitate internally, rather than externally, driven patterns in DG and CA3.

Our data provided strong support for those possibilities. Suppressing SST^+ interneurons amplified FG power in CA1 and DG, an effect specific to this interneuron class (Figure 6A–B and S5D). Interestingly, locally in DG and CA3, SG and FG showed an inverse relationship, where animals with the greatest SG suppression showed the greatest FG enhancement and vice versa (Figure S4E). This suggests that these two signatures of input drive may be opposing, with modulations that decrease SG power leading to greater FG power. Overall, these bidirectional changes in SG and FG power led to decreased SG/FG power ratios in CA1 following SST^+ suppression and increased SG/FG power ratios throughout the hippocampus following PV^+ suppression. These SG/FG ratio effects were significantly different between genotypes across the hippocampus (Figure 6C–E and S4F). FG coherence, however, did not change (Figure 6F). In addition, suppressing SST^+ interneurons increased FG frequency throughout the hippocampus (Figure 6G and S4G). Finally, suppressing SST^+ interneurons increased theta modulation of FG in CA1 (Figure 6H–J and S4H), an effect specific to SST^+ interneurons. Overall, suppressing SST^+ interneurons increased CA1 FG activity – a signature of EC drive – while suppressing PV^+ interneurons had opposing or no effects. These effects are consistent with a role for CA3 input as a modulator of FG in CA1.

Suppressing PV^+ or SST^+ interneurons unidirectionally modulates theta during movement

Next, we asked whether PV^+ and SST^+ interneurons might regulate theta. Previous work has suggested that theta throughout the hippocampus is driven in part by EC, but not by CA3 inputs (Colgin, 2016; Middleton and McHugh, 2016). Consequently, we predicted that suppressing SST^+ interneurons would enhance theta power in DG and CA3 only, perhaps through ungating EC inputs, while suppressing PV^+ interneurons would have no effect. Contrary to our hypothesis, suppressing either PV^+ or SST^+ interneurons increased theta power in CA1 but not elsewhere (Figure S5A–B). Neither interneuron type modified theta coherence (Figure S5C) or theta frequency (Figure S5D) save for an increase in theta frequency in PV-Cre mice in DG. These findings suggest that a general increase in CA3 spiking output increases CA1 theta power.

Overall, suppressing PV^+ interneurons in DG and CA3 increased measures of CA3 coupling onto CA1, including enhancing SG power, coherence, and theta comodulation and dampening FG-theta comodulation. In contrast, suppressing SST^+ interneurons in DG and CA3 increased measures of EC coupling onto CA1, including enhancing FG power and theta coupling and dampening SG power and theta coupling. Suppressing either interneuron type enhanced CA1 theta power.

Suppressing both PV^+ and SST^+ interneurons increases CA3 coupling onto CA1

Lastly, we assessed the effect of suppressing both interneuron populations simultaneously in PV-Cre/SST-Cre mice (Figure S6 and S7 and Table S5). Ablating AMPA currents to all hippocampal interneurons increases SWR rate and frequency (Caputi et al., 2012), similar to DG and CA3 PV^+ interneuron suppression (Figure 3C and 3F). Consistent with this result, we were unable to detect a difference between suppressing both interneuron types and suppressing PV+ interneurons only except in the case of comodulation of SG by theta in DG and CA3. In this instance, suppressing both interneuron types decreased theta modulation

of SG, an effect not observed when suppressing either type alone. In contrast, suppressing both interneuron types had largely distinct effects from suppressing SST+ interneurons only. The exceptions were FG frequency and CA1 FG power, in which case suppressing both interneuron types followed the direction of suppressing SST+ interneurons alone.

Consistency of effect across genotypes and sexes

To assess the robustness of these effects, we first assessed both males and females, since females have more DG interneurons than males at this age (Leung et al., 2012). Females had slightly larger SWR sizes than males during vehicle treatment epochs (Table S6), but there were otherwise no sex differences. The effect of suppressing interneurons was in the same direction and magnitude in both sexes on most features (Table S7) with a few exceptions. Suppressing SST^+ interneurons decreased SW amplitude in females but had the opposite effect in males, leading to no effect overall, and enhanced FG power to a greater degree in females than in males. Interestingly, suppressing either or both interneuron classes led to a greater increase in DG and CA3 MUA during movement in females. With those exceptions, the observed effects do not appear to be driven mainly in animals of a particular sex.

We further verified that differences in LFP during movement were not due to differences in running speed (vehicle 4.8 cm/s vs CNO 5.1 cm/s, paired t test, $t(29) = 1.31$, $p = 0.2$). We also confirmed that none of these effects could be confounded by differences between genotypes during vehicle treatment sessions (Table S4). We did note, however, that PV-Cre had different DG and CA3 SG frequencies and SG/FG ratios from SST-Cre mice during vehicle treatment (Table S4), but since the direction of this difference was opposite from the direction of treatment effect, it does not affect our interpretation. Finally, to control for possible off-target effects of CNO, we treated mice injected with an empty vector as a control and observed no differences between vehicle and CNO treated epochs (Figure S5 and S6 and Table S5).

DISCUSSION

We carried out targeted inhibition of PV^+ or SST^+ interneurons in the DG and CA3 regions of the hippocampus and found clear evidence for differential effects on activity in downstream CA1. Our findings provide evidence that PV^+ and SST^+ interneurons in DG and CA3 differentially regulate information flow through the hippocampus: suppression of PV^+ interneurons increased signatures of internal drive associated with CA3 input to CA1 while suppression of SST^+ interneurons increased signatures of external drive associated with EC input to CA1 (Figure 7). These bidirectional effects were observed despite both interneuron classes increasing the spiking output of DG and CA3 without changing spiking rates in CA1.

Specifically, suppressing PV^+ interneurons led to SWR and SG/FG modulation consistent with increased CA3 drive and decreased EC drive to CA1: SWRs seen during immobility had higher incidence, faster frequency, greater amplitude of coincident SWs and SG, and showed higher SG coherence across regions; SG during movement had greater power and coherence across regions while FG during movement had reduced modulation by theta. These findings concur with two recent studies which modulated CA3 PV^+ interneurons

in rats and *ex vivo* (Antonoudiou et al., 2020; López-Madrona et al., 2020). By contrast, suppressing SST^+ interneurons led to SWR and SG modulation consistent with decreased CA3 drive and increased EC drive to CA1: SWRs were less common and longer; SG during movement had reduced modulation by theta and FG during movement had greater power. Changes in LFP signatures in DG and CA3 were largely consistent with those seen in CA1, suggesting these patterns of activity changed locally and then propagated to CA1.

The roles we identified for DG and CA3 interneuron are remarkably similar to those identified for CA1 interneurons, where PV^+ interneurons regulate CA3 drive and SST^+ interneurons regulate EC drive (Fernández-Ruiz et al., 2017; Udakis et al., 2020). We therefore hypothesize that across the hippocampus, PV^+ and SST^+ interneurons could be modulated as different flows of information are needed.

Importantly, clear differences were observed following inhibition of the two interneuron subtypes despite the existence of substantial variation within interneuron classes (Harris et al., 2018; Klausberger and Somogyi, 2008). For example, PV^+ CA3 and DG interneurons are largely basket cells and axoaxonic cells, which both synapse near the soma, but which in CA1 differently couple to theta and SWRs (Klausberger and Somogyi, 2008). SST^+ interneurons are largely oriens-lacunsoum moleculare cells in CA3 and hilar-perforant pathway cells in DG, which both synapse at distal dendrites, but there are also several classes of CA3 and DG SST^+ projection neurons that target DG, EC, septum, and contralateral hippocampus (Honoré et al., 2021). There are also populations of PV and SST co-expressing cells (Jinno and Kosaka, 2000), most commonly bistratified cells (Tukker et al., 2007) which synapse onto proximal dendrites. Despite this diversity, our findings suggest overarching roles for PV^+ and SST^+ interneurons in DG and CA3 in regulating information flow through the hippocampal network.

We also identified a dissociation between overall activity levels in CA3 and signatures of CA3 drive in CA1. Suppressing SST^+ interneurons led to an increase CA3 input to CA1 as measured by CA3 MUA and CA1 stratum radiatum CSD. Despite that increase, we observed a decrease in signatures of CA3 input to CA1 but an increase in FG, a signature of direct EC input to CA1 (Colgin, 2016). Importantly, this dissociation between activity and influence is are consistent with the observation of reduced FG signatures of EC drive to CA1 following CA3 silencing (Middleton and McHugh, 2016). Thus, FG in CA1, rather than a pure signature of EC drive to CA1, is likely best understood as a signature of overall EC drive to both CA1 and the upstream DG and CA3 network. More broadly, these findings highlight the likely importance of specific patterns of CA3 spiking in influencing CA1: suppression of both interneuron types lead to increases in CA3 output but opposite effects on CA3- versus EC-associated LFP patterns in CA1. This is most likely a result of the engagement of different patterns of CA3 spiking.

In controlling input drive, these interneuron classes may regulate hippocampal information processing. The hippocampus contributes to encoding, consolidation, and retrieval of memories, and is thought to alternate between three distinct network states in order to do so (Buzsáki, 1989; Kay and Frank, 2019; Sosa et al., 2018). Encoding of new information is driven by external inputs from the EC, consolidation of previous information by internal

inputs from the CA3, and retrieval by a combination of EC and CA3 inputs (Carr and Frank, 2012). Thus, interneuron-mediated alterations in the strengths of these two inputs could help support different memory functions. Consistent with this possibility, previous behavioral studies examining DG and CA3 PV^+ and SST^+ interneurons during contextual threat conditioning support the hypothesis that PV^+ interneuron suppression could support consolidation by ungating internal CA3 input while SST^+ interneuron suppression could support encoding by ungating external EC input (Guo et al., 2018; Stefanelli et al., 2016; Zou et al., 2016). In sum, the hippocampal circuit may engage or disengage PV^+ and SST^+ interneurons during appropriate learning phases to alter the balance between CA3 and EC inputs and thereby support consolidation or encoding processes.

Previous studies of the CA1 LFP signatures further illustrate how DG and CA3 PV^+ and SST^+ interneurons might modulate learning and memory processes. First, suppressing SST^+ interneurons reduced SWR rate, which might reduce learning, as abolishing SWRs disrupts learning (Ego-Stengel and Wilson, 2010; Girardeau et al., 2009; Jadhav et al., 2012) and lower SWR rate predicts memory impairments in Alzheimer's models(Jones et al., 2019). However, we found that suppressing SST^+ interneurons also lengthened SWRs, which may increase the length of the underlying replay trajectory, which could facilitate learning in some cases (Fernández-Ruiz et al., 2019). In contrast, suppressing PV^+ interneurons increased fast ripple incidence, which may be a pathological conversion from SWRs (Behrens et al., 2007; Foffani et al., 2007) which in turn could disrupt normal encoding (Ewell et al., 2019). However, suppressing PV^+ interneurons heightened the extent to which SG coherence increased during SWRs, which is associated with greater replay fidelity (Carr et al., 2012). Finally, suppressing PV^+ interneurons increased SG power, which could support retrieval following task learning (Muzzio et al., 2009; Tort et al., 2009), while suppressing SST^+ interneurons increased FG power and modulation by theta, which could support encoding of new locations (Zheng et al., 2016) and working memory maintenance (Axmacher et al., 2010). Future experiments should examine if there is a casual relationship between activity of these GABAergic populations and spatial task performance.

SST^+ interneurons in the DG are specifically lost in Alzheimer's disease and normal aging models, and the extent of their loss correlates with memory impairments (Andrews-Zwilling et al., 2010; Leung et al., 2012; Spiegel et al., 2013). These models show reduced SWR rate, frequency, and coincident SG power (Cayzac et al., 2015; Ciupek et al., 2015; Cowen et al., 2018; Gillespie et al., 2016; Iaccarino et al., 2016; Nicole et al., 2016; Wiegand et al., 2016), and the extent of these impairments predicts memory deficits (Jones et al., 2019). Suppression of DG and CA3 SST^+ interneurons induces similar changes in SWR characteristics, serving as further evidence that loss of these interneurons may be directly responsible for SWR alterations in pathological and normal aging and related memory deficits.

Beyond the hippocampus, many other brain regions facilitate multiple information processing roles through a balance of inputs. This could also be modulated by PV^+ and SST^+ interneurons, as they have been shown to have distinct and often bidirectional roles in cortex. Specifically, this is found in tuning (Miao et al., 2017; Wilson et al., 2012), beta and theta frequency activity (Chen et al., 2017), stimulus-induced gamma rhythms (Hakim

et al., 2018; Veit et al., 2017), slow waves and spindles (Funk et al., 2017; Kuki et al., 2015; Niethard et al., 2018), NREM (Funk et al., 2017), reward encoding (Kvitsiani et al., 2013), and working memory (Abbas et al., 2018; Kim et al., 2016). These results are broadly consistent with our results showing bidirectional modulation of signatures of internal and external inputs by DG and CA3 PV^+ and SST^+ interneuron populations, and we suggest that the distinction between internal and external drive may be useful in understanding the roles of these interneurons outside the hippocampus.

Limitations of the Study

One main limitation of our study relates to the fact that we targeted interneurons in DG and CA3 together rather than separately. As described in the Methods, we initially aimed to target only DG, but found that across a variety of approaches we saw expression in both DG and CA3. This is consistent with previous studies that show expression in both regions when one or the other was targeted. (El-Gaby et al., 2021; Stefanelli et al., 2016; Twarkowski et al., 2021). This suggests that additional genetic specificity will be required to target interneurons in one subregion or the other.

STAR METHODS

RESOURCE AVAILABILITY

Lead Contact—Further information and requests for resources and reagents should be directed to and will be fulfilled by the Lead Contact, Loren Frank (loren.frank@uscf.edu).

Materials Availability—This study did not generate any unique reagents.

Data and Code Availability—0–300 Hz filtered LFP, MUA spike times, mouse position tracking, and metadata for each electrode site, mouse, and recording session have been deposited in the DANDI archive (https://gui.dandiarchive.org/#/dandiset/000165/draft) and are publicly available as of the date of publication. The permanent link is listed in the key resources table.

All original code has been deposited on Github and archived on Zenodo (https://doi.org/10.5281/zenodo.5618979) and is publicly available as of the date of publication. The DOI is listed in the key resources table.

Any additional information required to reanalyze the data reported in this paper is available from the lead contact upon request.

EXPERIMENTAL MODEL AND SUBJECT DETAILS

C57BL6/J mice with the SST-IRES-Cre allele (*Sst*$^{tm2.1(cre)Zjh}$/J) or the PV-IRES-Cre allele (*Pvalb*$^{tm1(cre)Arbr}$/J) knocked-in (Hippenmeyer et al., 2005; Taniguchi et al., 2011) were originally obtained from Jackson Laboratory. Equal numbers of PV-Cre, SST-Cre and PV-Cre/SST-Cre mice were selected from littermates of a PV-Cre x SST-Cre cross. All animals were bred in-house using trio breeding producing 10 pups per litter on average, which were weaned at 28 days. Equal proportions of males and females aged 3–8 months were selected for each genotype and viral vector. Within each genotype group and sex, mice

were randomly assigned to receive either hM4Di-mCherry vector or mCherry empty vector injection. Experimenters were blinded to genotype during surgery and blinded to genotype and viral vector expression during all post-operative behavior, recordings, and histology. Animals were housed in a pathogen-free barrier facility on a 12h light cycle (lights on at 7am and off at 7pm) at 19–23°C and 30–70% humidity. Animals were identified by ear punch under brief isofluorane anesthesia and genotyped by PCR of a tail clipping at both weaning and perfusion. All animals otherwise received no procedures except those reported in this study. Throughout the study, mice were singly housed. All animal experiments were conducted in accordance with the guidelines and regulations of the National Institutes of Health, the University of California, and the Gladstone Institutes under IACUC protocol AN117112.

METHOD DETAILS

This study consisted of three cohorts. The first cohort (n = 5 PV-Cre, n = 4 SST-Cre) had home cage recordings (Figure 2). This limited cohort was used exclusively for CSD analysis and thus was not included in the supplementary analyses in Tables S4–7. The second cohort (n = 9 PV-Cre, n = 10 SST-Cre, n = 6 PV-Cre/SST-Cre) had home cage recordings (Figure 3). The third cohort (n = 8 PV-Cre, n = 7 SST-Cre, n = 7 PV-Cre/SST-Cre, and n = 8 empty vector mice) had linear track recordings (Figure 5), then home cage recordings (Figure 3). In the third cohort, 1 PV-Cre and 1 SST-Cre animal died between linear track and home cage recordings and so were not included in the analysis in Figure 3 and Table S2.

Surgery—Mice were anesthetized by intraperitoneal injection of ketamine (60 mg/kg) and xylazine (30 mg/kg); anesthesia was maintained with 0.6–1.5% isofluorane given through a vaporizer and nose cone. The head was secured with earbars and a tooth bar in a stereotaxic alignment system (Kopf Instruments). Fur was removed from the scalp, which was then sterilized with alternating swabs of chlorhexidine and 70% ethanol. The scalp was opened, sterilized with 3% hydrogen peroxide, and thoroughly cleaned to reduce risk of tissue regrowth. 0.5 mm craniotomies were made at 1.95 mm AP and ± 1.5 mm ML from bregma for viral injection. 1 μL of 4.6×10^{12}vg/mL AAV5-hSyn-DIO-hM4D(Gi)-mCherry (UNC Viral Vector Core; (Krashes et al., 2011)) or 7×10^{12}vg/mL AAV5-hSyn-DIO-mCherry (Addgene) was injected at 2.1 mm below the surface of the brain (Andrews-Zwilling et al., 2012; Stefanelli et al., 2016) at an infusion rate of 100nL/min. Skull screws (FST) were inserted into craniotomies over the right frontal cortex and left parietal cortex to anchor and support the implant, and were secured with dental adhesive (C&B Metabond, Parkell). An additional 0.5 mm craniotomy was made over the right cerebellum for insertion of the indifferent ground and reference wires. The craniotomy centered at −1.95 mm AP and 1.5 mm ML from bregma and extended bidirectionally along the ML axis to 2 mm width to receive the recording probe. The probes had four 5 mm shanks spaced 400 μm apart with 8 electrode sites per shank and 200 μm spacing between sites (Neuronexus; configuration A4×8-5mm-400-200-703-CM32). For cohort 3, the probes had 1 6 mm shank with 32 sites and 50 μm spacing between sites (Neuronexus; configuration A1×32-6mm-50-703-CM32). The probe was quickly lowered until the tip reached 2.2 mm below the surface of the brain, and the reference and ground wire was inserted into the subdural space above the cerebellum. The probe was cemented in place with dental acrylic and the scalp was closed

with nylon sutures. Mice were treated with 0.0375 mg/kg buprenorphine intraperitoneally and 5 mg/kg ketofen subcutaneously 30–45 min after surgery, monitored until ambulatory, then monitored daily for 3 days. A minimum of 3 weeks was allowed for recovery and viral expression before recording.

We note here that although this injection site targets the DG, expression was seen throughout the DG and CA3. We used the same virus, titer, injection speed, volume, and coordinates as a previous study which targeted DG (Stefanelli et al., 2016) and observed DG and CA3 expression, just as in the original study. We also made a substantial effort to adapt this protocol to target DG and CA3 inhibitory populations independently and found that each of five different injection configurations assessed either had negligible expression or spread across DG and CA3. Given previous results showing similar spread to both DG and CA3, (El-Gaby et al., 2021; Stefanelli et al., 2016; Twarkowski et al., 2021), it seems that current viruses cannot target either region independently.

Electrophysiology—Each animal was randomly assigned a time during the light cycle, and behavior and recordings were always conducted with that animal at that same time each day ± 1 hour. CNO (NIMH, C-929) in 1% DMSO in 0.9% sterile saline (CNO) or equivalent volume of 1% DMSO in 0.9% sterile saline (vehicle) was administered via intraperitoneal injection at a dose of 2 mg/kg 1 hour prior to data collection. Body weight was measured weekly during treatment and injection volume was adjusted accordingly. Injections were well tolerated and had no adverse effects on health. Data were collected on a Main Control Unit (SpikeGadgets) with simultaneous video tracking at 30 frames/s using Trodes software (SpikeGadgets).

During home cage recordings, data were collected, amplified, multiplexed, processed, and digitized using a 32-channel upright headstage and commutator (SpikeGadgets) at 30 kHz. Data were collected during 60 min home cage sessions for 6 days, alternating vehicle and CNO administration. Home cages were changed to Alpha-dri bedding (Shepherd Specialty Papers) to enable video tracking.

For linear track recordings, animals were screened for sufficient food motivation prior to surgery. Each animal was restricted to 85–90% of its baseline weight then run on a 36 cm linear track for 30 min sessions daily for 10 μL soy milk reward dispensed from custom automatic solenoids controlled by an Environmental Control Unit (SpikeGadgets) with custom scripts. Animals which did not achieve at least 180 pokes over 3 sessions were excluded from surgery. Following surgery, animals ran for 30 min on linear track for 6 days, alternating vehicle and CNO administration. Data were collected, amplified, multiplexed, processed, and digitized using a wireless 32-channel mini logger headstage (SpikeGadgets) at 20 kHz.

Histology—Mice were deeply anesthetized with avertin, and a 30 μA current was passed through each recording site for 2 s (1 s for cohort 3) to generate small electrolytic lesions (Ugo Basile). Mice were then perfused with 0.9% NaCl. The brains were removed and stored at 4°C, then fixed in 4% PFA for 2 days, rinsed in PBS for 1 day, and cryoprotected in 30% sucrose for at least 2 days. Brains were cut into 30 μm coronal sections with a

microtome (Leica) and stored in cryoprotectant at −20°C. Every third section was stained with cresyl violet, then electrolytic lesion locations were observed under a light microscope at 5x magnification (Leica). Every tenth section was used for immunohistochemistry (about 12 sections per mouse). Sections were blocked and permeabilized in 10% normal donkey serum and 0.5% Triton X for 1 hour at room temperature, and then incubated overnight at 4°C in 1:100 rat anti-SST (Millipore), 1:1000 mouse anti-PV (Millipore), and 1:500 biotinylated rabbit anti-RFP (Abcam). For cohort 3, sections were incubated in 1 drop Mouse on Mouse Blocking Reagent (VectorLabs) per 4mL PBS for 1 hour prior to primary antibody incubation, and 1:100 mouse anti-SST (Santa Cruz) was used. Sections were then incubated for 1 hour at room temperature in 1:1500 donkey anti-rat AlexaFluor488 (Thermo Fisher Scientific) or 1:1500 goat anti-rat AlexaFluor647 (Thermo Fisher Scientific), 1:1500 donkey anti-mouse AlexaFluor647 (Thermo Fisher Scientific), and 1:1000 Streptavidin AlexaFluor594 (Sigma Aldrich) and mounted to slides using ProLong Gold with DAPI. Images were collected at 10x magnification on a fluorescent microscope (Keyence) and counted manually in ImageJ. Each section was manually confirmed to contain no sections with mCherry expression outside of DG or CA3. 1 SST-Cre animal from the first cohort was excluded from all analyses due to low viral expression (fewer than 50 mCherry+ cells). Representative images were adjusted for contrast only.

***Ex vivo* electrophysiology—**3–6 month old mice were stereotaxically injected with hM4D as described above, then the scalp was sutured closed. 3 weeks following surgery to allow for viral expression, mice were deeply anesthetized with isofluorane. The brain was rapidly removed and placed in 4°C slicing solution comprised of 110 mM Choline Chloride, 2.5 mM KCl, 1.25 mM NaH_2PO_4, 26 mM $NaHCO_3$, 2 mM $CaCl_2$, 1.3 mM Na Pyruvate, 1 mM L-Ascorbic Acid, and 10 mM dextrose. 300μm sagittal sections were cut using a vibratome (VT 1200s, Leica), transferred to a vapor interface chamber aerated with 95% O_2 / 5% CO_2 gas mixture, and allowed to recover at 34°C for one hour prior to recording. Sections were then transferred to a submerged recording chamber at 34°C perfused at 10 mL/min with oxygenated aCSF solution comprised of 124 mM NaCl, 26 mM $NaHCO_3$, 10 mM Glucose, 1.25 mM NaH_2PO_4, 2.5 mM KCl, 1.25 mM $MgCl_2$, and 1.5 mM $CaCl_2$. SST^+ and PV^+ cells were visually identified in the DG by mCherry expression and morphology using a modified Olympus BXW-51 microscope (Scientifica, Inc). Interneurons were recorded using patch-clamp electrodes filled with an intracellular solution comprised of 125 mM K-gluconate, 10 mM KCl, 10 mM HEPES, 2 mM $MgCl_2$, 10 mM EGTA, 4 mM MgATP, 10 mM Na-phosphocreatine, and 3 mM Na_2GTP. CNO was dissolved to 1μM in aCSF and delivered through the perfusion system. Whole cell recordings were performed using a Multiclamp 700B amplifier (Molecular Devices). The signals were sampled at 10 kHz and digitized using Digidata 1550B with Axon pCLAMP (Molecular Devices). Data was analyzed using custom scripts in IGOR Pro (WaveMetrics).

Analysis of neural data—Neural data was analyzed with custom software written in MATLAB (Mathworks) with the Chronux toolbox (http://www.chronux.org) and Trodes to MATLAB software (SpikeGadgets). The anatomical location of each electrode site was determined by examining Nissl-stained histological sections, raw LFP traces, the SWR-triggered spectrogram signature, and dentate spikes. Only DG sites with visually confirmed

dentate spikes were included in analysis. Data were data were referenced to a corpus callosum electrode which would exclude EMG artefacts, band-pass Butterworth filtered at 0.1–300 Hz, and then downsampled to 1 kHz and analyzed as LFP.

Raw LFP data during rest sessions were band-pass equiripple filtered at 125–200 Hz for SWRs, 0–30 Hz for SWs, and 30–50 Hz for SG. SWRs were detected on the CA1 site (or CA3 site, for Figure S3) closest to the center of the pyramidal layer and defined by the Hilbert envelope of the ripple-filtered trace, smoothed with a 4 ms Gaussian, exceeding 3 SD above baseline for at least 15 ms (Cheng and Frank, 2008). Analysis was restricted to periods of extended immobility, after the mouse Gaussian smoothed velocity had been < 1 cm/s for 30 seconds or more. SWRs were considered part of chains if a second SWR event occurred within 200 ms of the end of an event. Instantaneous frequency was defined by interpeak times during SWRs. SW amplitude was defined as the maximum absolute value of the Hilbert envelope of the SW-filtered trace during SWRs.

SWR-triggered spectrograms for each electrode site and SWR-triggered coherence between regions were calculated with the multitaper method, as previously described (Carr et al., 2012), with a 100 ms sliding window. Delta coherence was calculated as the difference between the 100 ms window starting 400 ms before SWR onset and the 100 ms window after SWR onset; SWRs that were preceded by SWRs within this window were excluded. For illustration in figures, a 10 ms sliding window was used. SWR-associated SG power was calculated as the averaged z-scored power over the 30–50 Hz frequency band 0–100 ms after ripple detection. SG power was analyzed for three regions: CA1-sr, CA3 including pyr and sr, and DG including hilus and granule cell layers. For CNO epochs, the mean and SD of the SG filtered signal from the vehicle epoch recorded the day before were used for z-scoring.

CSD was calculated by taking the second spatial derivative of the LFP following smoothing with a triangular kernel (Freeman and Nicholson, 1975). CSD units are arbitrary because tissue impedance was not measured. CSD was quantified by calculating the peak source and sink of the CSD in CA1-sr during the 100 ms following SWR onset.

For MUA analysis, data were referenced to a corpus callosum electrode, band-pass filtered at 600–6000 Hz (Butterworth), and then events greater than 75 μV were treated as spikes. Sites used for SWR detection were further verified to be in the CA1 pyramidal layer as they showed large increases in MUA during SWRs. The site closest to the center of the cell layer, as determined by highest MUA, was used for MUA analysis. For fast ripple analysis, data were downsampled to 5 kHz and band-pass equiripple filtered at 125–600 Hz, then events were detected in CA1 when the Hilbert envelope of the ripple-filtered trace, smoothed with a 4 ms Gaussian, exceeded 3 SD above baseline for at least 3 oscillations of the filtered trace. Events were classified as fast ripples if the mean frequency was above 250 Hz.

Dentate spikes were detected as previously described (Dvorak et al., 2021) at the site with the highest MUA and visually confirmed dentate spikes. Raw LFP during rest sessions were band-pass equiripple filtered at 5–100 Hz and z-score normalized, then peaks were detected. Amplitude was calculated as the difference between each peak and the closest minimum and length calculated as the time between the minima before and after each peak. The log of the

amplitudes were z-score normalized, then peaks were classified as dentate spikes if they had amplitudes > 0.75 and a duration between 5 and 25 ms. Analysis was restricted to periods of extended immobility, after the mouse Gaussian smoothed velocity had been < 1 cm/s for 30 seconds or more. Site spacing was too large for CSD analysis, thus dentate spikes were not classified by type (Dvorak et al., 2021).

Slow and fast gamma bands were defined by the frequencies with highest cross-frequency coupling, as previously described (Colgin et al., 2009; Kemere et al., 2013). Raw LFP during linear track sessions were then band-pass least squares FIR filtered at 5–11 Hz for theta, 20–50 Hz for SG, and 50–110 Hz for FG; these definitions matched those previously defined in mice using time-frequency methods (Cabral et al., 2014; Chen et al., 2011). Analysis was restricted to periods when the mouse Gaussian smoothed velocity exceeded 1 cm/s. Spectrograms were calculated with a multitaper method with a 1 s sliding window. Coherence was calculated using a multitaper method over all run periods. Instantaneous frequency was defined by interpeak times of the band filtered trace during all run periods. LFP during run epochs was analyzed for 5 regions: CA1 pyr, sr, and slm; CA3 including pyr and sr; and DG including hilus and granule cell layers.

QUANTIFICATION AND STATISTICAL ANALYSIS

Statistics were computed using custom software written in MATLAB (Mathworks). Figures S6–S7 were plotted with plotSpread function (MATLAB Central File Exchange). Statistical test used, exact n, and exact p value are in figure legends; test statistic values and degrees of freedom are in corresponding supplementary tables. In all cases, n represents number of animals. No data were excluded based on statistical tests. 3 mice were excluded from analysis due to poor viral expression. Sample sizes were based on previous studies (Gan et al., 2017; Lovett-Barron et al., 2014; Stefanelli et al., 2016; Xia et al., 2017). Central values plotted in Figures 2–6 and S1–S5 are means and individual points are mean per animal, as indicated in figure legends. Central values plotted in Figures S6–S7 are linear mixed effects model (LMM) fixed effect coefficients $\beta \pm 95\%$ confidence intervals and individual points are the fitted conditional response for each mouse, as indicated in figure legends.

Data for LMMs were drawn from events in the case of SWRs, time bins in the case of continuous measures (1 min for SWR rate, 100 ms for MUA, 1 s for all others), or peaks in the case of continuous frequency. Normality and independence of errors was confirmed visually; when errors were not Gaussian, they were always right skewed, and so a log transform was applied. We constructed an LMM using the ML method and the formula *feature ~ group + (group|animal)* where group was vehicle or CNO for treatment comparison, PV-Cre or SST-Cre for vehicle baselines comparison, and male or female for sex comparison. We then used an F test to assess the evidence that the treatment fixed effect model was a better fit than the intercept-only model. To evaluate differences between treatment effects, we pooled data across two groups and used a likelihood ratio test to compare the model *feature ~ treatment + (treatment|animal)* to the model *feature ~ treatment:gentoype + (treatment:genotype|animal)* (or *feature ~ treatment:sex + (treatment:sex|animal)* in the case of Table S6) and used a χ^2 test to assess if the data were equally likely under both models. For table S1, we used paired t tests when data were

normally distributed as shown by Shapiro-Wilk test and variances between groups were similar as shown by F test; we used Wilcoxon matched pairs signed rank tests otherwise. For correlations in Figures S2 and S4, data were normally distributed as shown by Shapiro-Wilk test, so we used Pearson correlations.

Significance threshold was set by the Holm-Bonferroni correction across an experiment with $\alpha = 0.05$. Other family-wise error rate correction methods were tested with similar results. An experiment was defined as all comparisons made during either rest sessions (24 comparisons in Figures 2–4 and S2–3) or run sessions (36 comparisons in Figures 5, 6, and S4–5) in a single genotype or between genotypes. Only p-values that met this threshold are displayed as significant in figures and tables.

Supplementary Material

Refer to Web version on PubMed Central for supplementary material.

ACKNOWLEDGEMENTS

This work was supported by the National Science Foundation Graduate Research Fellowship No. 1144247, National Institute on Aging Predoctoral Fellowship No. F31AG057150, and Genentech Foundation Fellowship to E.A.A.J, funding from the Howard Hughes Medical Institutes to L.M.F., and National Institute on Aging grants RF1AG047655, RF1AG055421, R01AG055682, and P01AG073082 to Y.H. We thank Eric Denovellis for assistance with designing the linear mixed effects model, and Max Liu and Scott Owen for assistance with linear track construction, and Alex Gonzalez and Abhilasha Joshi for manuscript feedback.

REFERENCES

Abbas AI, Sundiang MJM, Henoch B, Morton MP, Bolkan SS, Park AJ, Harris AZ, Kellendonk C, and Gordon JA (2018). Somatostatin Interneurons Facilitate Hippocampal-Prefrontal Synchrony and Prefrontal Spatial Encoding. Neuron 100, 926–939.e3. [PubMed: 30318409]

Andrews-Zwilling Y, Bien-Ly N, Xu Q, Li G, Bernardo A, Yoon SY, Zwilling D, Yan TX, Chen L, and Huang Y (2010). Apolipoprotein E4 causes age- and Tau-dependent impairment of GABAergic interneurons, leading to learning and memory deficits in mice. J Neurosci 30, 13707–13717. [PubMed: 20943911]

Andrews-Zwilling Y, Gillespie AK, Kravitz AV, Nelson AB, Devidze N, Lo I, Yoon SY, Bien-Ly N, Ring K, Zwilling D, et al. (2012). Hilar GABAergic interneuron activity controls spatial learning and memory retrieval. PLoS One 7, e40555. [PubMed: 22792368]

Antonoudiou P, Tan YL, Kontou G, Upton AL, and Mann EO (2020). Parvalbumin and Somatostatin Interneurons Contribute to the Generation of Hippocampal Gamma Oscillations. J. Neurosci 40, 7668–7687. [PubMed: 32859716]

Axmacher N, Henseler MM, Jensen O, Weinreich I, Elger CE, and Fell J (2010). Cross-frequency coupling supports multi-item working memory in the human hippocampus. Proc. Natl. Acad. Sci 107, 3228–3233. [PubMed: 20133762]

Behrens CJ, van den Boom LP, and Heinemann U (2007). Effects of the $GABA_A$ receptor antagonists bicuculline and gabazine on stimulus-induced sharp wave-ripple complexes in adult rat hippocampus *in vitro*. Eur. J. Neurosci 25, 2170–2181. [PubMed: 17419756]

Blasco-Ibáñez JM, and Freund TF (1995). Synaptic Input of Horizontal Interneurons in Stratum Oriens of the Hippocampal CA1 Subfield: Structural Basis of Feed-back Activation. Eur. J. Neurosci 7, 2170–2180. [PubMed: 8542073]

Bragin A, Jandó G, Nádasdy Z, van Landeghem M, and Buzsáki G (1995a). Dentate EEG spikes and associated interneuronal population bursts in the hippocampal hilar region of the rat. J. Neurophysiol 73, 1691–1705. [PubMed: 7643175]

Bragin A, Jandó G, Nádasdy Z, Hetke J, Wise K, Buzsáki G, Szabó G, Freund TF, and Hájos N (1995b). Gamma (40–100 Hz) oscillation in the hippocampus of the behaving rat. J. Neurosci 15, 47–60. [PubMed: 7823151]

Buzsáki G (1989). Two-stage model of memory trace formation: A role for "noisy" brain states. Neuroscience 31, 551–570. [PubMed: 2687720]

Buzsáki G, Leung L, and Vanderwolf CH (1983). Cellular bases of hippocampal EEG in the behaving rat. Brain Res. 287, 139–171. [PubMed: 6357356]

Buzsáki G, Horváth Z, Urioste R, Hetke J, and Wise K (1992). High-frequency network oscillation in the hippocampus. Science 256, 1025–1027. [PubMed: 1589772]

Cabral HO, Vinck M, Fouquet C, Pennartz CMA, Rondi-Reig L, and Battaglia FP (2014). Oscillatory dynamics and place field maps reflect hippocampal ensemble processing of sequence and place memory under NMDA receptor control. Neuron 81, 402–415. [PubMed: 24462101]

Caputi A, Fuchs EC, Allen K, Le Magueresse C, and Monyer H (2012). Selective Reduction of AMPA Currents onto Hippocampal Interneurons Impairs Network Oscillatory Activity. PLoS One 7, e37318. [PubMed: 22675480]

Carr MF, and Frank LM (2012). A single microcircuit with multiple functions: state dependent information processing in the hippocampus. Curr. Opin. Neurobiol 22, 704–708. [PubMed: 22480878]

Carr MF, Karlsson MP, and Frank LM (2012). Transient Slow Gamma Synchrony Underlies Hippocampal Memory Replay. Neuron 75, 700–713. [PubMed: 22920260]

Cayzac S, Mons N, Ginguay A, Allinquant B, Jeantet Y, and Cho YH (2015). Altered hippocampal information coding and network synchrony in APP-PS1 mice. Neurobiol. Aging 36, 3200–3213. [PubMed: 26391642]

Chen G, Zhang Y, Li X, Zhao X, Ye Q, Lin Y, Tao HW, Rasch MJ, and Zhang X (2017). Distinct Inhibitory Circuits Orchestrate Cortical beta and gamma Band Oscillations. Neuron 96, 1403–1418.e6. [PubMed: 29268099]

Chen Z, Resnik E, McFarland JM, Sakmann B, and Mehta MR (2011). Speed Controls the Amplitude and Timing of the Hippocampal Gamma Rhythm. PLoS One 6, e21408. [PubMed: 21731735]

Cheng S, and Frank LM (2008). New experiences enhance coordinated neural activity in the hippocampus. Neuron 57, 303–313. [PubMed: 18215626]

Ciupek SM, Cheng J, Ali YO, Lu H-C, and Ji D (2015). Progressive Functional Impairments of Hippocampal Neurons in a Tauopathy Mouse Model. J. Neurosci 35, 8118–8131. [PubMed: 26019329]

Colgin LL (2015). Theta-gamma coupling in the entorhinal-hippocampal system. Curr. Opin. Neurobiol 31, 45–50. [PubMed: 25168855]

Colgin LL (2016). Rhythms of the hippocampal network. Nat. Rev. Neurosci 17, 239–249. [PubMed: 26961163]

Colgin LL, Denninger T, Fyhn M, Hafting T, Bonnevie T, Jensen O, Moser M-B, and Moser EI (2009). Frequency of gamma oscillations routes flow of information in the hippocampus. Nature 462, 353–357. [PubMed: 19924214]

Cowen SL, Gray DT, Wiegand J-PPL, Schimanski LA, and Barnes CA (2018). Age-associated changes in waking hippocampal sharp-wave ripples. Hippocampus 30, 28–38. [PubMed: 29981255]

Csicsvari J, Hirase H, Mamiya A, and Buzsáki G (2000). Ensemble patterns of hippocampal CA3-CA1 neurons during sharp wave-associated population events. Neuron 28, 585–594. [PubMed: 11144366]

Drexel M, Romanov RA, Wood J, Weger S, Heilbronn R, Wulff P, Tasan RO, Harkany T, and Sperk G (2017). Selective Silencing of Hippocampal Parvalbumin Interneurons Induces Development of Recurrent Spontaneous Limbic Seizures in Mice. J. Neurosci 37, 8166–8179. [PubMed: 28733354]

Dvorak D, Chung A, Park EH, and Fenton AA (2021). Dentate spikes and external control of hippocampal function. Cell Rep. 36, 109497. [PubMed: 34348165]

Ego-Stengel V, and Wilson MA (2010). Disruption of ripple-associated hippocampal activity during rest impairs spatial learning in the rat. Hippocampus 20, 1–10. [PubMed: 19816984]

El-Gaby M, Reeve HM, Lopes-dos-Santos V, Campo-Urriza N, Perestenko PV, Morley A, Strickland LAM, Lukács IP, Paulsen O, and Dupret D (2021). An emergent neural coactivity code for dynamic memory. Nat. Neurosci 24, 694–704. [PubMed: 33782620]

Ewell LA, Fischer KB, Leibold C, Leutgeb S, and Leutgeb JK (2019). The impact of pathological high-frequency oscillations on hippocampal network activity in rats with chronic epilepsy. Elife 8, e42148. [PubMed: 30794155]

Fernández-Ruiz A, Oliva A, Nagy GA, Maurer AP, Berényi A, and Buzsáki G (2017). Entorhinal-CA3 Dual-Input Control of Spike Timing in the Hippocampus by Theta-Gamma Coupling. Neuron 93, 1213–1226.e5. [PubMed: 28279355]

Fernández-Ruiz A, Oliva A, Fermino de Oliveira E, Rocha-Almeida F, Tingley D, and Buzsáki G (2019). Long-duration hippocampal sharp wave ripples improve memory. Science 364, 1082–1086. [PubMed: 31197012]

Foffani G, Uzcategui YG, Gal B, Menendez de la Prida L, Szabo I, Sik A, Buzsáki G, Wilent WB, and Higley MJ (2007). Reduced Spike-Timing Reliability Correlates with the Emergence of Fast Ripples in the Rat Epileptic Hippocampus. Neuron 55, 930–941. [PubMed: 17880896]

Freeman JA, and Nicholson C (1975). Experimental optimization of current source density technique for anuran cerebellum. J. Neurophysiol 38, 369–382. [PubMed: 165272]

Freund TF, and Buzsáki G (1996). Interneurons of the hippocampus. Hippocampus 6, 347–470. [PubMed: 8915675]

Funk CM, Peelman K, Bellesi M, Marshall W, Cirelli C, and Tononi G (2017). Role of Somatostatin-Positive Cortical Interneurons in the Generation of Sleep Slow Waves. J. Neurosci 37, 9132–9148. [PubMed: 28821651]

Gan J, Weng S, Pernía-Andrade AJ, Csicsvari J, and Jonas P (2017). Phase-Locked Inhibition, but Not Excitation, Underlies Hippocampal Ripple Oscillations in Awake Mice In Vivo. Neuron 93, 308–314. [PubMed: 28041883]

Gillespie AK, Jones EA, Lin Y-H, Karlsson MP, Kay K, Yoon SY, Tong LM, Nova P, Carr JS, Frank LM, et al. (2016). Apolipoprotein E4 causes age-dependent disruption of slow gamma oscillations during hippocampal sharp-wave ripples. Neuron 90, 740–751. [PubMed: 27161522]

Girardeau G, Benchenane K, Wiener SI, Buzsáki G, and Zugaro MB (2009). Selective suppression of hippocampal ripples impairs spatial memory. Nat. Neurosci 12, 1222–1223. [PubMed: 19749750]

Gulyás AI, Megías M, Emri Z, Freund TF, Whittington M, and Buzsáki G (1999). Total number and ratio of excitatory and inhibitory synapses converging onto single interneurons of different types in the CA1 area of the rat hippocampus. J. Neurosci 19, 10082–10097. [PubMed: 10559416]

Guo N, Soden ME, Herber C, Kim MT, Besnard A, Lin P, Ma X, Cepko CL, Zweifel LS, and Sahay A (2018). Dentate granule cell recruitment of feedforward inhibition governs engram maintenance and remote memory generalization. Nat. Med 24, 438–449. [PubMed: 29529016]

Hakim R, Shamardani K, and Adesnik H (2018). A neural circuit for gamma-band coherence across the retinotopic map in mouse visual cortex. Elife 7, e28569. [PubMed: 29480803]

Harris KD, Hochgerner H, Skene NG, Magno L, Katona L, Bengtsson Gonzales C, Somogyi P, Kessaris N, Linnarsson S, and Hjerling-Leffler J (2018). Classes and continua of hippocampal CA1 inhibitory neurons revealed by single-cell transcriptomics. PLOS Biol. 16, e2006387. [PubMed: 29912866]

Hippenmeyer S, Vrieseling E, Sigrist M, Portmann T, Laengle C, Ladle DR, and Arber S (2005). A developmental switch in the response of DRG neurons to ETS transcription factor signaling. PLoS Biol. 3, e159. [PubMed: 15836427]

Honoré E, Khlaifia A, Bosson A, and Lacaille JC (2021). Hippocampal Somatostatin Interneurons, Long-Term Synaptic Plasticity and Memory. Front. Neural Circuits 15, 687558. [PubMed: 34149368]

Iaccarino HF, Singer AC, Martorell AJ, Rudenko A, Gao F, Gillingham TZ, Mathys H, Seo J, Kritskiy O, Abdurrob F, et al. (2016). Gamma frequency entrainment attenuates amyloid load and modifies microglia. Nature 540, 230–235. [PubMed: 27929004]

Jadhav SP, Kemere C, German PW, and Frank LM (2012). Awake Hippocampal Sharp-Wave Ripples Support Spatial Memory. Science 336, 1454–1458. [PubMed: 22555434]

Jinno S, and Kosaka T (2000). Colocalization of parvalbumin and somatostatin-like immunoreactivity in the mouse hippocampus: Quantitative analysis with optical disector. J. Comp. Neurol 428, 377–388. [PubMed: 11074441]

Jinno S, and Kosaka T (2002). Patterns of expression of calcium binding proteins and neuronal nitric oxide synthase in different populations of hippocampal GABAergic neurons in mice. J. Comp. Neurol 449, 1–25. [PubMed: 12115690]

Jinno S, and Kosaka T (2003). Patterns of expression of neuropeptides in GABAergic nonprincipal neurons in the mouse hippocampus: Quantitative analysis with optical disector. J. Comp. Neurol 461, 333–349. [PubMed: 12746872]

Jones EA, Gillespie AK, Yoon SY, Frank LM, and Huang Y (2019). Early Hippocampal Sharp-Wave Ripple Deficits Predict Later Learning and Memory Impairments in an Alzheimer's Disease Mouse Model. Cell Rep 29, 2123–2133.e4. [PubMed: 31747587]

Kay K, and Frank LM (2019). Three brain states in the hippocampus and cortex. Hippocampus 29, 184–238. [PubMed: 29722465]

Kemere C, Carr MF, Karlsson MP, and Frank LM (2013). Rapid and continuous modulation of hippocampal network state during exploration of new places. PLoS One 8, e73114. [PubMed: 24023818]

Kim D, Jeong H, Lee J, Ghim J-W, Her ES, Lee S-H, and Jung MW (2016). Distinct Roles of Parvalbumin- and Somatostatin-Expressing Interneurons in Working Memory. Neuron 92, 902–915. [PubMed: 27746132]

Klausberger T, and Somogyi P (2008). Neuronal diversity and temporal dynamics: the unity of hippocampal circuit operations. Science 321, 53–57. [PubMed: 18599766]

Krashes MJ, Koda S, Ye C, Rogan SC, Adams AC, Cusher DS, Maratos-Flier E, Roth BL, and Lowell BB (2011). Rapid, reversible activation of AgRP neurons drives feeding behavior in mice. J. Clin. Invest 121, 1424–1428. [PubMed: 21364278]

Kuki T, Fujihara K, Miwa H, Tamamaki N, Yanagawa Y, and Mushiake H (2015). Contribution of parvalbumin and somatostatin-expressing GABAergic neurons to slow oscillations and the balance in beta-gamma oscillations across cortical layers. Front Neural Circuits 9, 1–12. [PubMed: 25713515]

Kvitsiani D, Ranade S, Hangya B, Taniguchi H, Huang JZ, and Kepecs A (2013). Distinct behavioural and network correlates of two interneuron types in prefrontal cortex. Nature 498, 363–366. [PubMed: 23708967]

Lee C-T, Kao M-H, Hou W-H, Wei Y-T, Chen C-L, and Lien C-C (2016). Causal Evidence for the Role of Specific GABAergic Interneuron Types in Entorhinal Recruitment of Dentate Granule Cells. Sci. Rep 6, 36885. [PubMed: 27830729]

Leung L, Andrews-Zwilling Y, Yoon SY, Jain S, Ring K, Dai J, Wang MM, Tong L, Walker D, and Huang Y (2012). Apolipoprotein E4 causes age- and sex-dependent impairments of hilar GABAergic interneurons and learning and memory deficits in mice. PLoS One 7, e53569. [PubMed: 23300939]

López-Madrona VJ, Pérez-Montoyo E, Álvarez-Salvado E, Moratal D, Herreras O, Pereda E, Mirasso CR, and Canals S (2020). Different theta frameworks coexist in the rat hippocampus and are coordinated during memory-guided and novelty tasks. Elife 9, e57313. [PubMed: 32687054]

Lovett-Barron M, Turi GF, Kaifosh P, Lee PH, Bolze F, Sun X-H, Nicoud J-F, Zemelman BV, Sternson SM, and Losonczy A (2012). Regulation of neuronal input transformations by tunable dendritic inhibition. Nat. Neurosci 15, 423–430. [PubMed: 22246433]

Lovett-Barron M, Kaifosh P, Kheirbek MA, Danielson N, Zaremba JD, Reardon TR, Turi GF, Hen R, Zemelman BV, and Losonczy A (2014). Dendritic inhibition in the hippocampus supports fear learning. Science 343, 857–863. [PubMed: 24558155]

Maurer AP, Cowen SL, Burke SN, Barnes CA, and McNaughton BL (2006). Phase precession in hippocampal interneurons showing strong functional coupling to individual pyramidal cells. J. Neurosci 26, 13485–13492. [PubMed: 17192431]

McKenzie S (2017). Inhibition shapes the organization of hippocampal representations. Hippocampus 28, 659–671. [PubMed: 28921762]

Miao C, Cao Q, Moser M-B, and Moser EI (2017). Parvalbumin and Somatostatin Interneurons Control Different Space-Coding Networks in the Medial Entorhinal Cortex. Cell 171, 507–521.e17. [PubMed: 28965758]

Middleton SJ, and McHugh TJ (2016). Silencing CA3 disrupts temporal coding in the CA1 ensemble. Nat. Neurosci 19, 945–951. [PubMed: 27239937]

Miles R, Tóth K, Gulyás AI, Hájos N, and Freund TF (1996). Differences between Somatic and Dendritic Inhibition in the Hippocampus. Neuron 16, 815–823. [PubMed: 8607999]

Muzzio IA, Levita L, Kulkarni J, Monaco J, Kentros C, Stead M, Abbott LF, and Kandel ER (2009). Attention Enhances the Retrieval and Stability of Visuospatial and Olfactory Representations in the Dorsal Hippocampus. PLoS Biol. 7, e1000140. [PubMed: 19564903]

Nakashiba T, Buhl DL, McHugh TJ, and Tonegawa S (2009). Hippocampal CA3 output is crucial for ripple-associated reactivation and consolidation of memory. Neuron 62, 781–787. [PubMed: 19555647]

Nicole O, Hadzibegovic S, Gajda J, Bontempi B, Bem T, and Meyrand P (2016). Soluble amyloid beta oligomers block the learning-induced increase in hippocampal sharp wave-ripple rate and impair spatial memory formation. Sci. Rep 6, 22728. [PubMed: 26947247]

Niethard N, Ngo H-VV, Ehrlich I, and Born J (2018). Cortical circuit activity underlying sleep slow oscillations and spindles. Proc. Natl. Acad. Sci 115, E9220–E9229. [PubMed: 30209214]

Oliva A, Fernández-Ruiz A, Fermino de Oliveira E, and Buzsáki G (2018). Origin of Gamma Frequency Power during Hippocampal Sharp-Wave Ripples. Cell Rep. 25, 1693–1700. [PubMed: 30428340]

Ormond J, McNaughton BL, and Moser EI (2015). Place field expansion after focal MEC inactivations is consistent with loss of Fourier components and path integrator gain reduction. Proc. Natl. Acad. Sci. U. S. A 112, 4116–4121. [PubMed: 25733884]

Penttonen M, Kamondi A, Sik A, Acsády L, and Buzsáki G (1997). Feed-forward and feed-back activation of the dentate gyrus in vivo during dentate spikes and sharp wave bursts. Hippocampus 7, 437–450. [PubMed: 9287083]

Ramirez-Villegas JF, Logothetis NK, and Besserve M (2015). Diversity of sharp-wave–ripple LFP signatures reveals differentiated brain-wide dynamical events. Proc. Natl. Acad. Sci 112, E6379–E6387. [PubMed: 26540729]

Ramirez-Villegas JF, Willeke KF, Logothetis NK, and Besserve M (2018). Dissecting the Synapse- and Frequency-Dependent Network Mechanisms of In Vivo Hippocampal Sharp Wave-Ripples. Neuron 100, 1224–1240.e13. [PubMed: 30482688]

Royer S, Zemelman BV, Losonczy A, Kim J, Chance F, Magee JC, and Buzsáki G (2012). Control of timing, rate and bursts of hippocampal place cells by dendritic and somatic inhibition. Nat. Neurosci 15, 769–775. [PubMed: 22446878]

Schlesiger MI, Cannova CC, Boublil BL, Hales JB, Mankin EA, Brandon MP, Leutgeb JK, Leibold C, and Leutgeb S (2015). The medial entorhinal cortex is necessary for temporal organization of hippocampal neuronal activity. Nat. Neurosci 18, 1123–1132. [PubMed: 26120964]

Sik A, Penttonen M, Ylinen A, Buzsáki G, Wise K, and Buzsáki G (1995). Hippocampal CA1 interneurons: an in vivo intracellular labeling study. J. Neurosci 15, 6651–6665. [PubMed: 7472426]

Sik A, Penttonen M, and Buzsáki G (1997). Interneurons in the Hippocampal Dentate Gyrus: an In Vivo intracellular Study. Eur. J. Neurosci 9, 573–588. [PubMed: 9104599]

Sosa M, Gillespie AK, and Frank LM (2018). Neural Activity Patterns Underlying Spatial Coding in the Hippocampus. In Current Topics in Behavioral Neuroscience, Volume 37, (Springer Berlin Heidelberg), pp. 43–100.

Spampanato J, and Dudek FE (2017). Targeted Interneuron Ablation in the Mouse Hippocampus Can Cause Spontaneous Recurrent Seizures. ENeuro 4, ENEURO.0130-17.2017.

Spiegel AM, Koh MT, Vogt NM, Rapp PR, and Gallagher M (2013). Hilar interneuron vulnerability distinguishes aged rats with memory impairment. J. Comp. Neurol 521, 3508–3523. [PubMed: 23749483]

Stark E, Roux L, Eichler R, Senzai Y, Royer SS, and Buzsáki G (2014). Pyramidal Cell-Interneuron Interactions Underlie Hippocampal Ripple Oscillations. Neuron 83, 467–480. [PubMed: 25033186]

Stefanelli T, Bertollini C, Lüscher C, Muller D, and Mendez P (2016). Hippocampal Somatostatin Interneurons Control the Size of Neuronal Memory Ensembles. Neuron 89, 1074–1085. [PubMed: 26875623]

Takács VT, Klausberger T, Somogyi P, Freund TF, and Gulyás AI (2012). Extrinsic and local glutamatergic inputs of the rat hippocampal CA1 area differentially innervate pyramidal cells and interneurons. Hippocampus 22, 1379–1391. [PubMed: 21956752]

Taniguchi H, He M, Wu P, Kim S, Paik R, Sugino K, Kvitsiani D, Fu Y, Lu J, Lin Y, et al. (2011). A resource of Cre driver lines for genetic targeting of GABAergic neurons in cerebral cortex. Neuron 71, 995–1013. [PubMed: 21943598]

Tort ABL, Komorowski RW, Manns JR, Kopell NJ, and Eichenbaum H (2009). Theta-gamma coupling increases during the learning of item-context associations. Proc. Natl. Acad. Sci. U. S. A 106, 20942–20947. [PubMed: 19934062]

Tukker JJ, Fuentealba P, Hartwich K, Somogyi P, and Klausberger T (2007). Cell type-specific tuning of hippocampal interneuron firing during gamma oscillations in vivo. J. Neurosci 27, 8184–8189. [PubMed: 17670965]

Twarkowski H, Steininger V, Kim MJ, and Sahay A (2021). A dentate gyrus-CA3 inhibitory circuit promotes evolution of hippocampal-cortical ensembles during memory consolidation. BioRxiv 2021.05.21.445117.

Udakis M, Pedrosa V, Chamberlain SEL, Clopath C, and Mellor JR (2020). Interneuron-specific plasticity at parvalbumin and somatostatin inhibitory synapses onto CA1 pyramidal neurons shapes hippocampal output. Nat. Commun 11, 4395. [PubMed: 32879322]

Valero M, Averkin RG, Fernandez-Lamo I, Aguilar J, Lopez-Pigozzi D, Brotons-Mas JR, Cid E, Tamas G, and Menendez de la Prida L (2017). Mechanisms for Selective Single-Cell Reactivation during Offline Sharp-Wave Ripples and Their Distortion by Fast Ripples. Neuron 94, 1234–1247.e7. [PubMed: 28641116]

Veit J, Hakim R, Jadi MP, Sejnowski TJ, and Adesnik H (2017). Cortical gamma band synchronization through somatostatin interneurons. Nat Neurosci 20, 951–959. [PubMed: 28481348]

Wheeler DW, White CM, Rees CL, Komendantov AO, Hamilton DJ, and Ascoli GA (2015). Hippocampome.org: a knowledge base of neuron types in the rodent hippocampus. Elife 4, e09960. [PubMed: 26402459]

Wiegand J-PL, Gray DT, Schimanski LA, Lipa P, Barnes CA, and Cowen SL (2016). Age Is Associated with Reduced Sharp-Wave Ripple Frequency and Altered Patterns of Neuronal Variability. J. Neurosci 36, 5650–5660. [PubMed: 27194342]

Wilson NR, Runyan CA, Wang FL, and Sur M (2012). Division and subtraction by distinct cortical inhibitory networks in vivo. Nature 488, 343–348. [PubMed: 22878717]

Wu F, Stark E, and Ku P (2015). Monolithically Integrated m LEDs on Silicon Neural Probes for High-Resolution Optogenetic Studies in Behaving Animals. Neuron 88, 1136–1148. [PubMed: 26627311]

Xia F, Richards BA, Tran MM, Josselyn SA, Takehara-Nishiuchi K, and Frankland PW (2017). Parvalbumin-positive interneurons mediate neocortical-hippocampal interactions that are necessary for memory consolidation. Elife 6, e27868. [PubMed: 28960176]

Yamamoto J, and Tonegawa S (2017). Direct Medial Entorhinal Cortex Input to Hippocampal CA1 Is Crucial for Extended Quiet Awake Replay. Neuron 96, 217–227.e4. [PubMed: 28957670]

Yamamoto J, Suh J, Takeuchi D, and Tonegawa S (2014). Successful execution of working memory linked to synchronized high-frequency gamma oscillations. Cell 157, 845–857. [PubMed: 24768692]

Ylinen A, Bragin A, Nádasdy Z, Jandó G, Szabó I, Sik A, and Buzsáki G (1995). Sharp wave-associated high-frequency oscillation (200 Hz) in the intact hippocampus: network and intracellular mechanisms. J. Neurosci 15, 30–46. [PubMed: 7823136]

Zheng C, Bieri KW, Hsiao Y-T, and Colgin LL (2016). Spatial Sequence Coding Differs during Slow and Fast Gamma Rhythms in the Hippocampus. Neuron 89, 398–408. [PubMed: 26774162]

Zou D, Chen L, Deng D, Jiang D, Dong F, McSweeney C, Zhou Y, Liu L, Chen G, Wu Y, et al. (2016). DREADD in parvalbumin interneurons of the dentate gyrus modulates anxiety, social interaction and memory extinction. Curr. Mol. Med 16, 91–102. [PubMed: 26733123]

Highlights

- Local field potential signatures of entorhinal cortex (EC) and CA3 coupling to CA1
- Suppressing DG and CA3 PV+ or SST+ neurons increases CA3 output to CA1
- Suppressing PV+ neurons increases CA3-CA1 coupling and decreases EC-CA1 coupling
- Suppressing SST+ neurons decreases CA3-CA1 coupling and increases EC-CA1 coupling

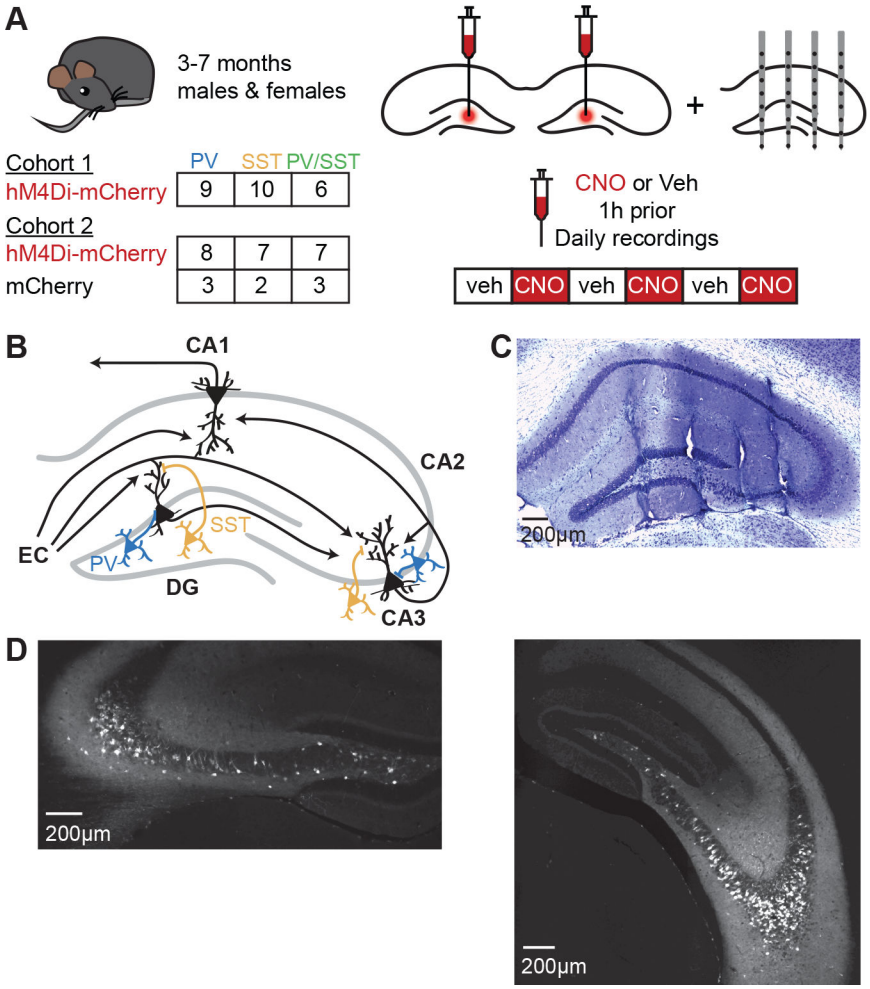

Figure 1. Recording *in vivo* hippocampal LFP during chemogenetic suppression of PV$^+$ and SST$^+$ interneurons in DG and CA3.

(A) Experimental strategy. Mice were bilaterally injected with AAV5-hSyn-DIO-hM4D(Gi)-mCherry or with AAV5-hSyn-DIO-mCherry into the DG hilus, then implanted with a 32-site 4-shank silicon electrode array into the right dorsal hippocampus. LFP activity was recorded from all hippocampal subregions over 6 daily 1 hour sessions, alternating CNO and vehicle treatment.

(B) Simplified circuit diagram of the hippocampus. DG and CA3 receive excitatory inputs from EC layer II onto distal dendrites and inhibitory inputs from local PV$^+$ interneurons (blue) onto the soma and local SST$^+$ interneurons (yellow) onto distal dendrites. CA1 receives direct input from EC layer III, indirect input from EC layer II via DG and CA3, and input from CA3. Adapted with permission from (Gillespie et al., 2016).

(C) Example cresyl violet stain of a dorsal hippocampal section showing a subset of electrode locations.

(D) Example of mCherry expression in dorsal (left) and ventral (right) hippocampus in a PVCre mouse and an SSTCre mouse, respectively.

Scale bars are 200 µm. See also Figure S1 and Table S1.

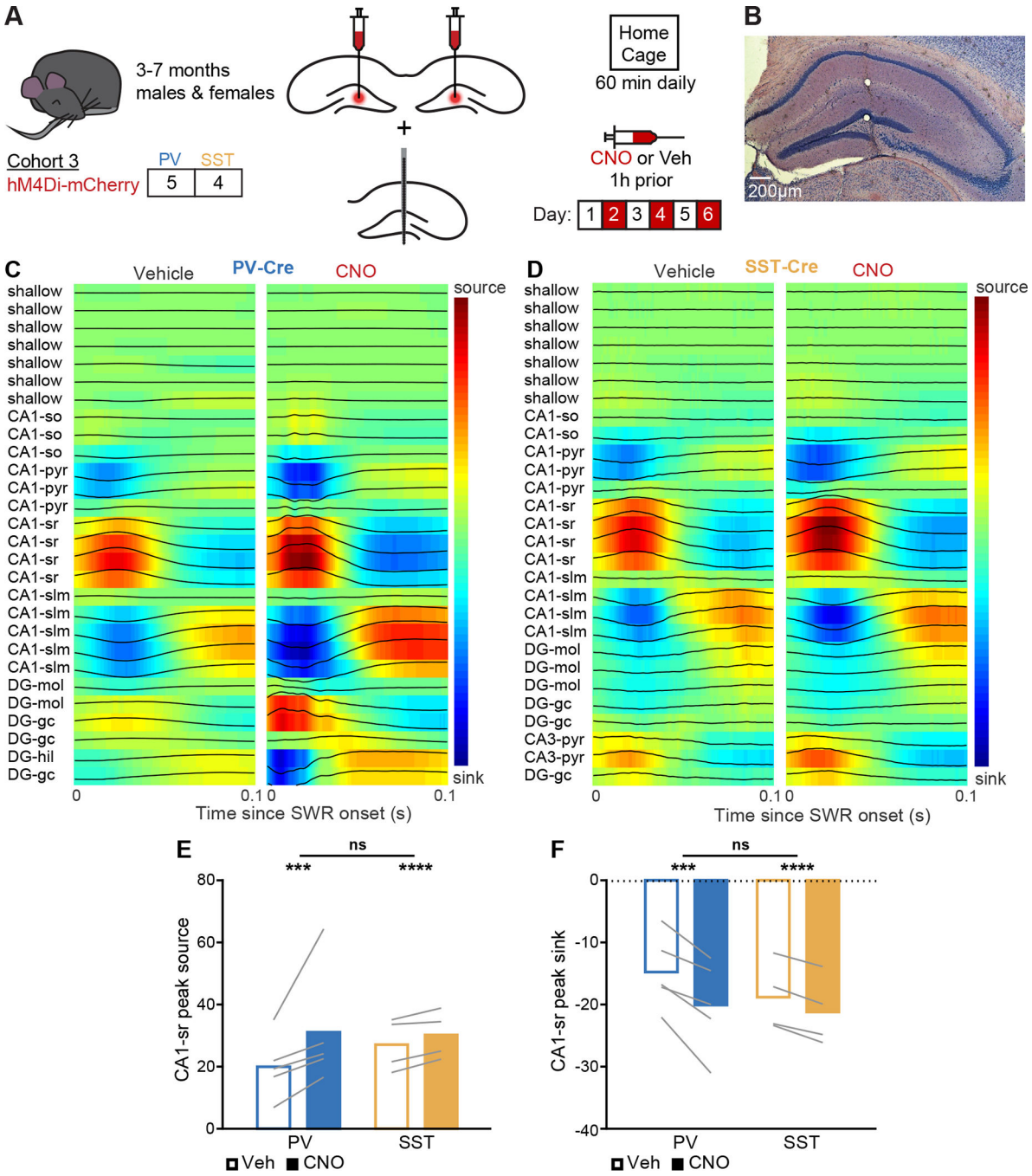

Figure 2. CSD in CA1-sr during SWRs increases following interneuron suppression.

(A) Experimental strategy. Mice were bilaterally injected with AAV5-hSyn-DIO-hM4D(Gi)-mCherry into the DG hilus, then implanted with a 32-site single-shank silicon electrode array into the right dorsal hippocampus. LFP activity was recorded during sleep and awake rest over 6 daily 1 hour home cage session, alternating CNO and vehicle treatment.

(B) Example cresyl violet stain of a dorsal hippocampal section showing a subset of electrode locations. Scale bar is 200 µm.

(C,D) Representative SWR-triggered CSD profiles across the entire electrode shank during vehicle-treated epochs (left) and CNO-treated epochs (right) in (C) a PV-Cre mouse and (D) an SST-Cre mouse, averaged over SWRs. Sites include those outside the hippocampus (shallow); CA1 strata oriens (CA1-so), pyramidale (CA1-pyr), radiatum (CA1-sr), and lacunosum moleculare (CA1-slm); DG granule cell layer (DG-gc) and hilus (DG-hil); and CA3 stratum pyramidale (CA3-pyr).

(E,F) Peak source (PV: $p = 0.00062$; SST: $p = 4.64\times10^{-5}$; PV vs SST: $p = 1$) and peak sink (PV: $p = 0.00013$; SST: $p = 1.24\times10^{-14}$; PV vs SST: $p = 1$) in CA1-sr during the 100 ms following SWR onset. Units are arbitrary because tissue impedance was not measured. N = 5 PV-Cre and n = 4 SST-Cre mice. Statistical details in Table S3. F test of the LMM for treatment effects, likelihood ratio test for genotype-treatment interaction effects. ***$p < 0.001$; ****$p < 0.0001$. Central values are means and individual points are mean per animal. See also Table S3.

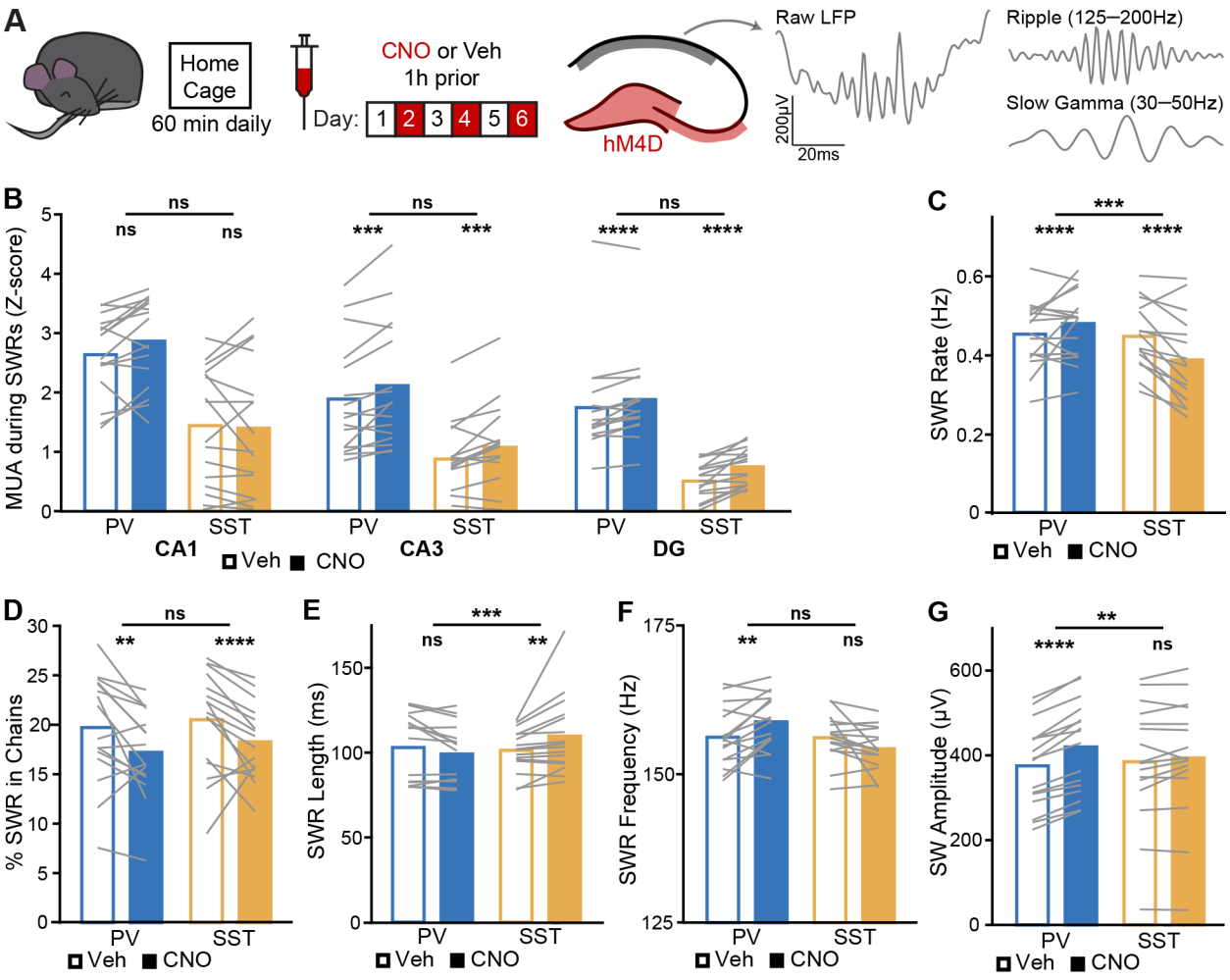

Figure 3. Suppressing PV$^+$ or SST$^+$ interneurons bidirectionally modulates SWR signatures of CA3 coupling to CA1.

(A) Mice were recorded during sleep and awake rest over 6 daily home cage sessions, alternating vehicle and CNO treatment. Interneurons in DG and CA3 (magenta) were inhibited while SWRs and related oscillations were assessed in CA1 stratum pyramidale (pyr) and stratum radiatum (sr) (grey). Representative raw, ripple filtered, and SG filtered traces of a SWR event from a CA1-pyr site of a PV-Cre/SST-Cre mouse during vehicle treatment.

(B) Normalized recruitment to SWRs of MUA in CA1 (PV: $p = 0.13$; SST: $p = 0.46$; PV vs SST: $p = 0.023$), CA3 (PV: $p = 0.00075$; SST: $p = 0.00076$; PV vs SST: $p = 0.095$), and DG (PV: $p = 5.5\times10^{-6}$; SST: $p = 3.4\times10^{-5}$; PV vs SST: $p = 0.059$).

(C) SWR rate (PV: $p = 1.9\times10^{-6}$; SST: $p = 4.6\times10^{-5}$; PV vs SST: $p = 0.00098$).

(D) Percent of SWRs following another SWR within 200 ms (PV: $p = 0.001$; SST: $p = 2.5\times10^{-5}$; PV vs SST: $p = 0.99$).

(E) SWR temporal length (PV: $p = 0.033$; SST: $p = 0.0023$; PV vs SST: $p = 0.00034$).

(F) SWR instantaneous frequency (PV: $p = 0.0012$; SST: $p = 0.033$; PV vs SST: $p = 0.018$).

(G) SW amplitude (PV: $p = 6.4\times10^{-27}$; SST: $p = 0.25$; PV vs SST: $p = 0.005$).

N = 16 PV-Cre and n = 16 SST-Cre mice. Statistical details in Table S3. F test of the LMM for treatment effects, likelihood ratio test for genotype-treatment interaction effects. **p < 0.01; ***p < 0.001; ****p < 0.0001. Central values are means and individual points are mean per animal. See also Figures S2, S3, S6, and S7 and Tables S2–S7.

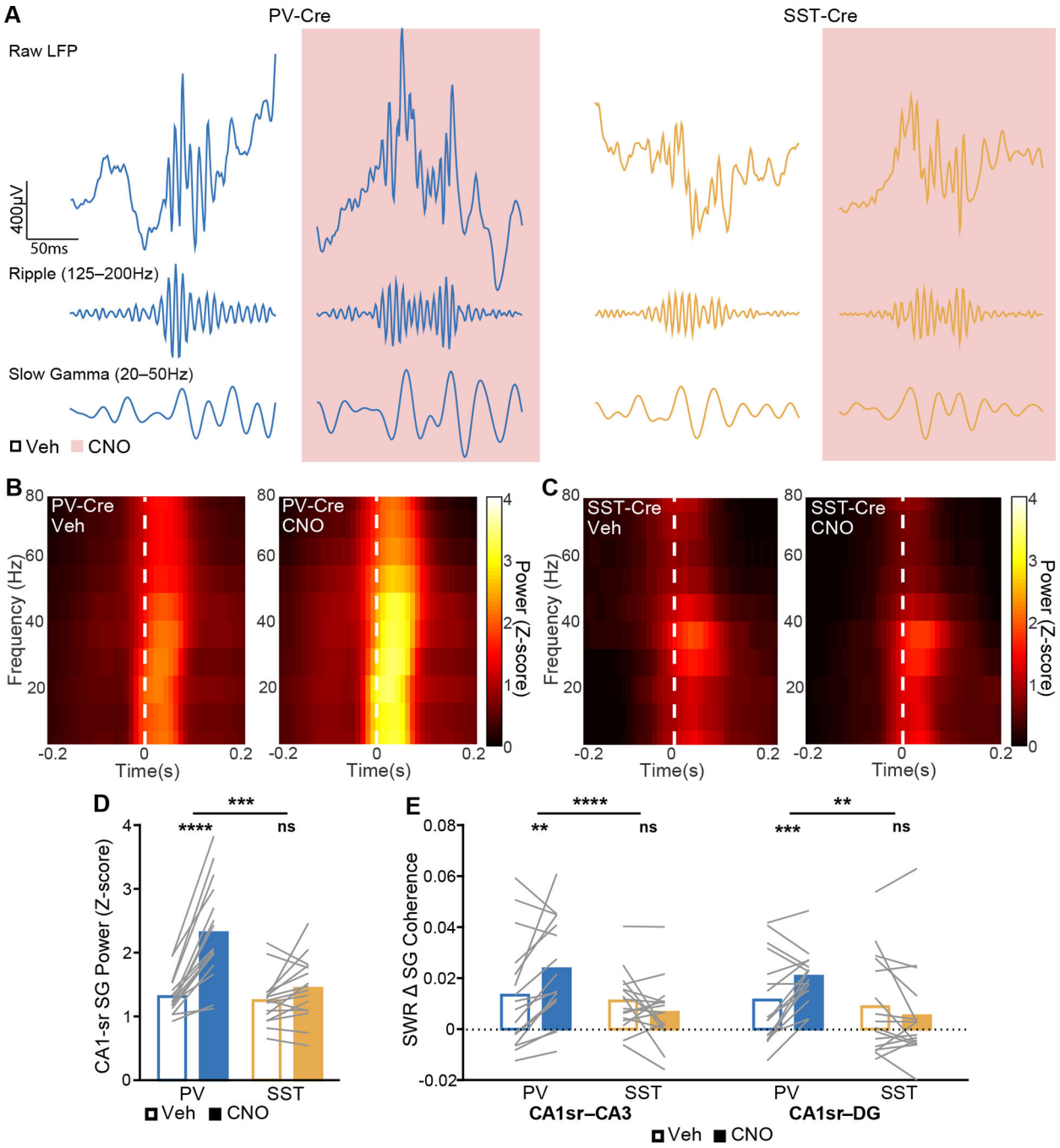

Figure 4. Suppressing PV$^+$ or SST$^+$ interneurons bidirectionally modulates SWR-coincident SG signatures of CA3 coupling to CA1.

(A) Example raw (top), SWR-filtered (middle), and SG-filtered (bottom) LFP traces from CA1 pyramidal layer sites from a PV-Cre (left) and an SST-Cre (right) mouse. SG power is higher both outside of and during SWRs in PV-Cre mice following CNO treatment.

(B,C) Representative SWR-triggered spectrograms from a CA1-sr layer site during vehicle-treated epochs (left) and CNO-treated epochs (right) in (A) a PV-Cre mouse and (B) an SST-Cre mouse, averaged over SWRs. White dash lines represent threshold crossing for SWR detection.

(D) Normalized SG power during SWRs in CA1 (PV: $p = 1.7\times10^{-23}$; SST: p = 0.14; PV vs SST: p = 0.00099).
(E) Increase during SWRs of SG frequency band coherence between CA1 and CA3 (PV: p = 0.0011; SST: p = 0.17; PV vs SST: $p = 9.4\times10^{-6}$) and between CA1 and DG (PV: p = 0.00097; SST: p = 0.43; PV vs SST: p = 0.0036).
N = 16 PV-Cre and n = 16 SST-Cre mice. Statistical details in Table S3. F test of the LMM for treatment effects, likelihood ratio test for genotype-treatment interaction effects. **p < 0.01; ***p < 0.001; ****p < 0.0001. Central values are means and individual points are mean per animal. See also Figures S2, S3, S6, and S7 and Tables S2–S7.

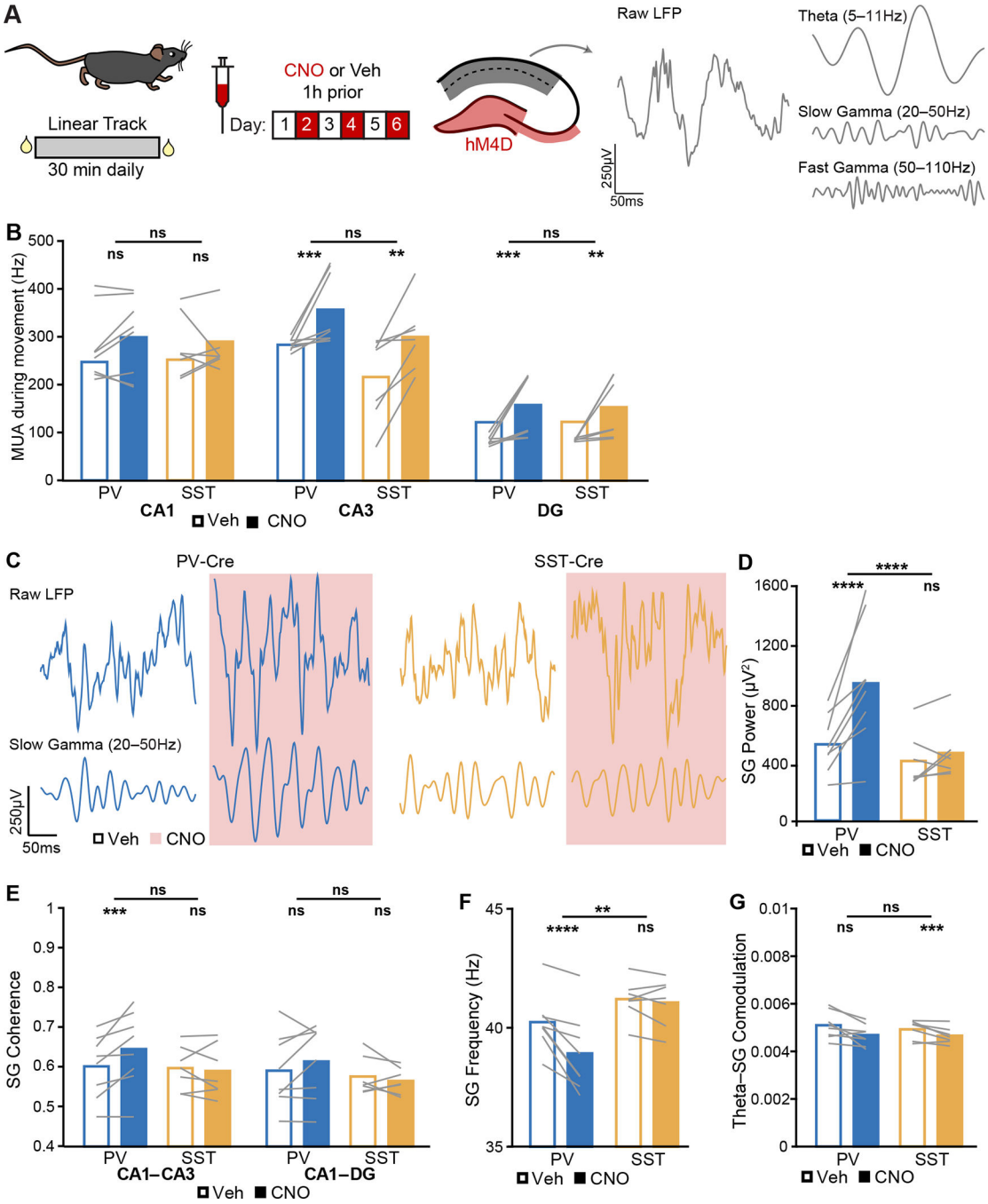

Figure 5. Suppressing PV$^+$ or SST$^+$ interneurons bidirectionally modulates SG signatures of CA3 coupling to CA1 during movement.

(A) Mice were recorded during linear track runs over 6 daily sessions, alternating vehicle and CNO treatment. Interneurons in DG and CA3 (magenta) were inhibited while theta and gamma oscillations were assessed in CA1-pyr, CA1-sr, and CA1 stratum lacunosum-moleculare (slm) (grey). Representative raw trace and LFP filtered for theta, SG, and FG from a CA1-pyr site of a PV-Cre mouse during movement during vehicle treatment.

(B) MUA during movement in CA1 (PV: p = 0.72; SST: p = 0.9; PV vs SST: p = 0.34), CA3 (PV: p = 0.00051; SST: p = 0.005; PV vs SST: p = 0.87), and DG (PV: p = 0.00022; SST: p = 0.0063; PV vs SST: p = 0.59).
(C) Example raw (top) and SG-filtered (bottom) LFP traces from CA1 pyramidal layer sites from a PV-Cre (left) and an SST-Cre (right) mouse.
(D) SG power in CA1 (PV: $p = 2.6\times10^{-6}$; SST: p = 0.13; PV vs SST: $p = 4.7\times10^{-6}$).
(E) SG frequency band coherence between CA1 and CA3 (PV: p = 0.00028; SST: p = 0.6; PV vs SST: p = 0.56) and between CA1 and DG (PV: p = 0.085; SST: p = 0.3; PV vs SST: p = 0.26).
(F) SG instantaneous frequency in CA1 (PV: $p = 2.5\times10^{-6}$; SST: p = 0.56; PV vs SST: p = 0.0061).
(G) Theta modulation of SG power in CA1 (PV: p = 0.12; SST: p = 0.00082; PV vs SST: p = 0.95).
N = 8 PV-Cre and n = 7 SST-Cre mice. Statistical details in Table S3. F test of the LMM for treatment effects, likelihood ratio test for genotype-treatment interaction effects. **p < 0.01; ***p < 0.001; ****p < 0.0001. Central values are means and individual points are mean per animal. See also Figures S4–S7 and Tables S3–S7.

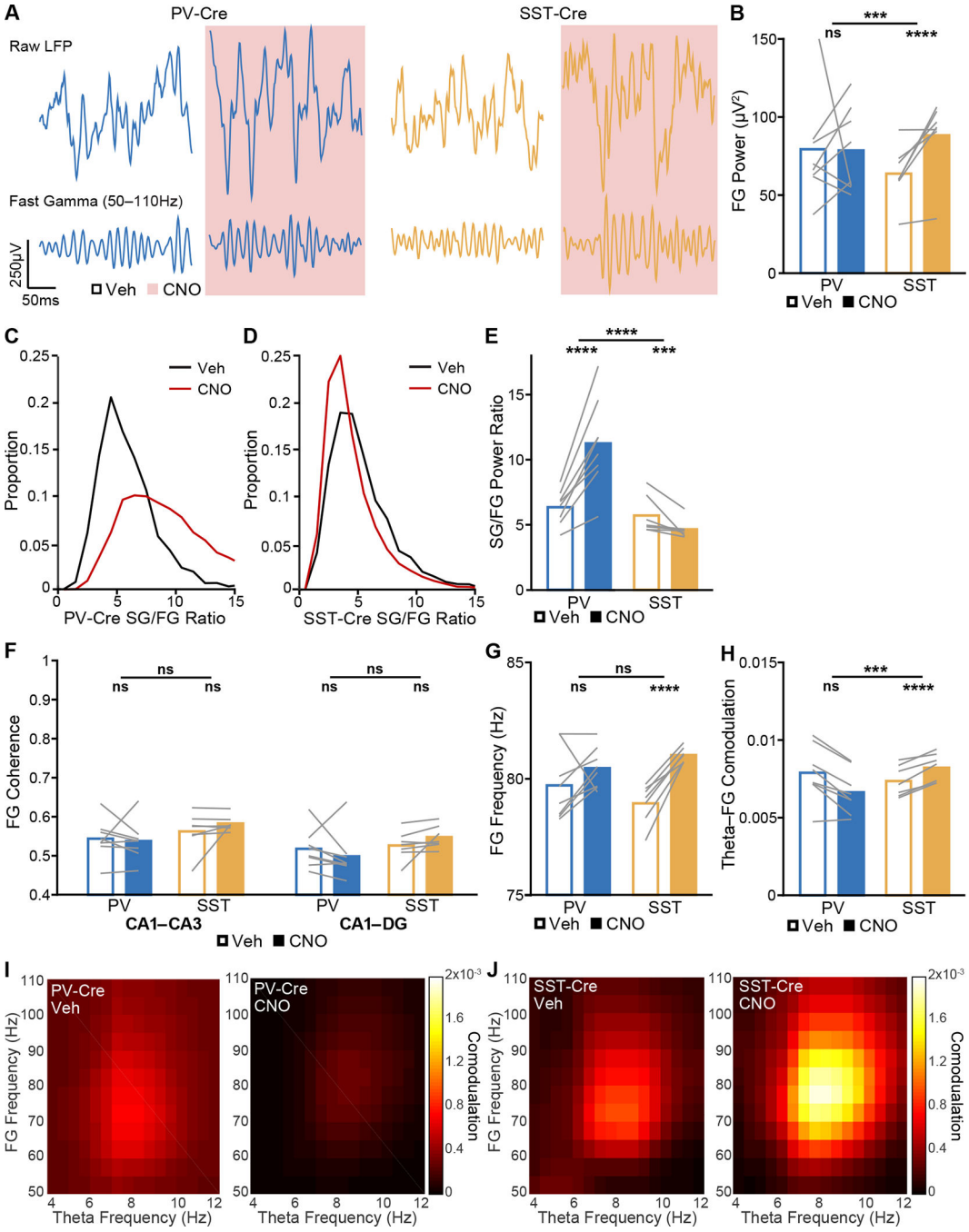

Figure 6. Suppressing PV$^+$ or SST$^+$ interneurons bidirectionally modulates FG signatures of EC coupling to CA1 during movement.

(A) Example raw (top) and FG-filtered (bottom) LFP traces from CA1 pyramidal layer sites from a PV-Cre (left) and an SST-Cre (right) mouse.

(B) FG power in CA1 (PV: $p = 0.27$; SST: $p = 3.3\times10^{-5}$; PV vs SST: $p = 0.00054$).

(C,D) Representative distributions of CA1 SG/FG power ratios over 1 s bins in (C) a PV-Cre mouse and (D) an SST-Cre mouse, averaged over CA1-pyr sites and time bins.

(E) Ratio of CA1 SG power to FG power (PV: $p = 9.7\times10^{-25}$; SST: $p = 0.00013$; PV vs SST: $p = 7.4\times10^{-6}$).

(F) FG frequency band coherence between CA1 and CA3 (PV: p = 0.83; SST: p = 0.2; PV vs SST: p = 0.24) and between CA1 and DG (PV: p = 0.27; SST: p = 0.076; PV vs SST: p = 0.47).
(G) FG instantaneous frequency in CA1 (PV: p = 0.06; SST: $p = 4.3\times10^{-17}$; PV vs SST: p = 0.065).
(H) Theta modulation of FG power in CA1 (PV: p = 0.0098; SST: $p = 8\times10^{-20}$; PV vs SST: p = 0.0001).
(I,J) Representative CA1 comodulograms during vehicle-treated epochs (left) and CNO-treated epochs (right) in a (I) a PV-Cre mouse and (J) an SST-Cre mouse, averaged over CA1-pyr sites and time bins.
N = 8 PV-Cre and n = 7 SST-Cre mice. Statistical details in Table S3. F test of the LMM for treatment effects, likelihood ratio test for genotype-treatment interaction effects. **p < 0.01; ***p < 0.001; ****p < 0.0001. Central values are means and individual points are mean per animal. See also Figures S4–S7 and Tables S3–S7.

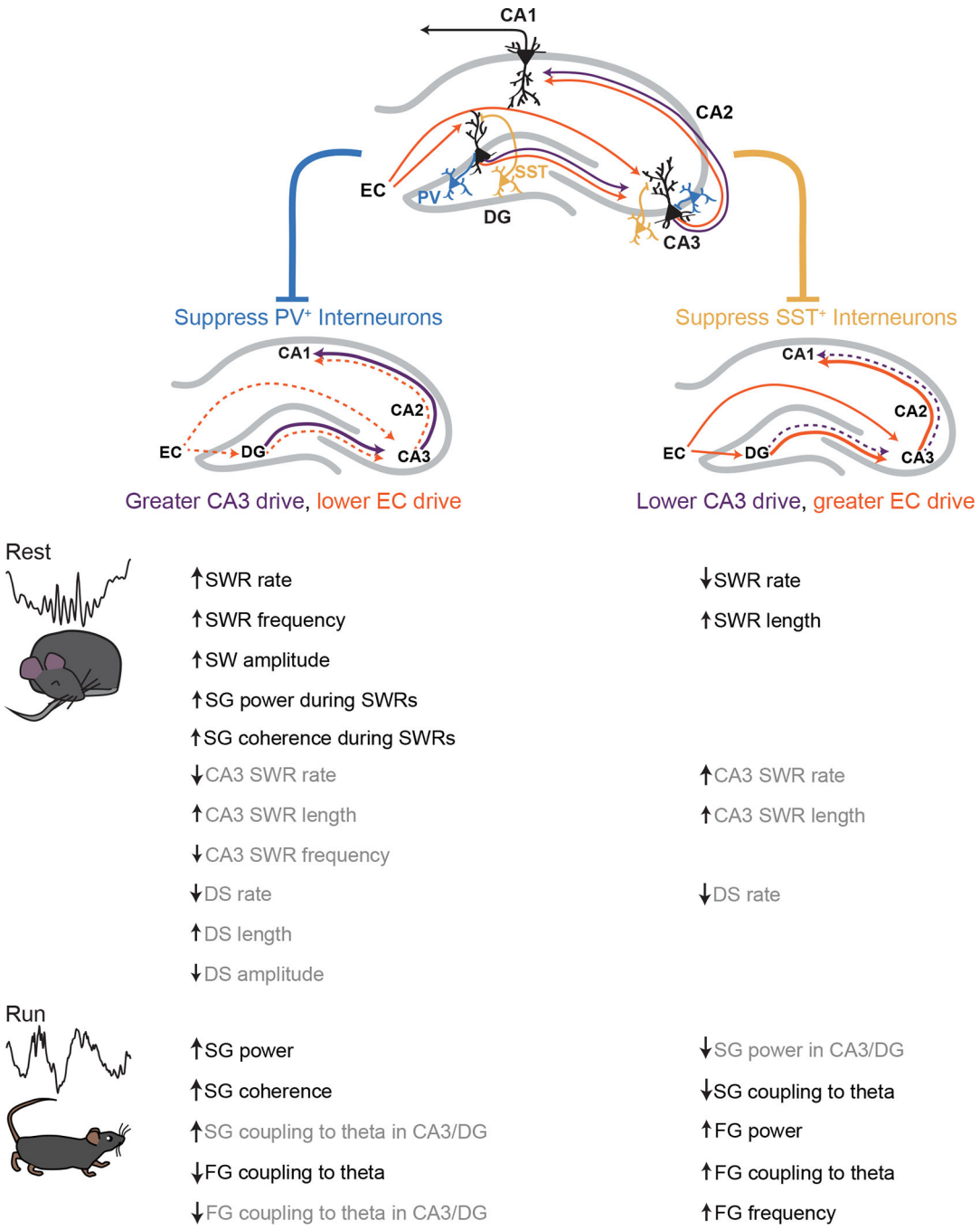

Figure 7. PV$^+$ and SST$^+$ interneurons in DG and CA3 bidirectionally modulate signatures of internal and external drive.

CA1 receives direct input from CA3 and indirect input from DG via CA3, and these regions in turn receive projections from EC layer II. PV$^+$ (blue) and SST$^+$ (yellow) interneurons in DG and CA3 appear to regulate the switch between greater CA3 drive to CA1 and greater EC drive to CA1. When PV$^+$ interneurons are suppressed, signatures of CA3 drive are enhanced and signatures of EC drive are curtailed. When SST$^+$ interneurons are suppressed, signatures of CA3 drive are curtailed and signatures of EC drive are enhanced. These manifest as changes to SWR, SW, and SG properties during rest periods and to theta, SG,

and FG during running periods both downstream in CA1 (black) or locally in DG and CA3 (grey). These interneurons may contribute to the modulation between these internal and external inputs to modulate memory representations.

KEY RESOURCES TABLE

REAGENT or RESOURCE	SOURCE	IDENTIFIER
Antibodies		
Rat anti-SST	Millipore	Cat#MAB354; RRID:AB_2255365
Mouse anti-SST	Santa Cruz	Cat#sc-7819; RRID: AB_2302603
Mouse anti-PV	Millipore	Cat#MAB1572; RRID:AB_2174013
Biotinylated rabbit anti-RFP	Abcam	Cat#ab34771; RRID:AB_777699
Donkey anti-rat AlexaFluor488	Thermo Fisher Scientific	Cat#A-21208; RRID:AB_2535794
Goat anti-rat AlexaFluor647	Thermo Fisher Scientific	Cat#A-21247; RRID:AB_141778
Donkey anti-mouse AlexaFluor647	Thermo Fisher Scientific	Cat#A-31571; RRID:AB_162542
Streptavidin AlexaFluor594	Sigma Aldrich	Cat#S6402
Bacterial and Virus Strains		
AAV5-hSyn-DIO-hM4D(Gi)-mCherry	UNC Viral Vector Core (Krashes et al., 2011)	RRID:Addgene_44362
AAV5-hSyn-DIO-mCherry	Addgene	RRID:Addgene_50459
Chemicals, Peptides, and Recombinant Proteins		
Ketamine	Henry Schein	Cat#1049007
Xylazine (Anased)	Henry Schein	Cat#1311139
Isofluorane	Henry Schein	Cat#029405
Buprenorphine	Henry Schein	Cat#055175
Ketofen	Henry Schein	Cat#005487
Avertin (2,2,2-Tribromoethanol)	Millipore Sigma	Cat# T48402
Dental Adhesive (Metabond)	Parkell	Cat#S396, S398 and S371
Dental Acrylic	Stoelting Co.	Cat#51459
Cresyl Violet Acetate	Sigma Aldrich	Cat#C5042
Mouse on Mouse Blocking Reagent	VectorLabs	Cat#MKB-2213-1
ProLong Gold with DAPI	Thermo Fisher Scientific	Cat#P36931
Deposited Data		
0–300 Hz filtered LFP, MUA spike times, mouse position tracking, and metadata for each electrode site, mouse, and recording session	This paper	https://gui.dandiarchive.org/#/dandiset/000165/draft
Experimental Models: Organisms/Strains		
Mouse: PVCre: *Pvalb*$^{tm1(cre)Arbr}$/J	Jackson Laboratory	MGI:3590684; RRID:IMSR_JAX:013044
Mouse: SSTCre: *Sst*$^{tm2.1(cre)Zjh}$/J	Jackson Laboratory	MGI:4838416; RRID:IMSR_JAX:008069
Software and Algorithms		
Custom scripts for this paper	This paper	https://doi.org/10.5281/zenodo.5618979
Trodes	SpikeGadgets	https://bitbucket.org/mkarlsso/trodes/downloads
NeuroQuery	Bitbucket	https://bitbucket.org/mkarlsso/neuroquery/src/master
MATLAB	Mathworks	N/A
Chronux	Cold Spring Harbor Laboratory	http://chronux.org

REAGENT or RESOURCE	SOURCE	IDENTIFIER
plot spread points	MATLAB Central File Exchange	https://www.mathworks.com/matlabcentral/fileexchange/37105-plot-spread-points-beeswarm-plot
Axon pCLAMP	Molecular Devices	https://mdc.custhelp.com/app/answers/detail/a_id/18779/~/axon%E2%84%A2pclamp%E2%84%A2-10-electrophysiology-data-acquisition-%26-analysis-software-download
IGOR Pro	WaveMetrics	https://www.wavemetrics.com/
Other		
Probe	Neuronexus	A4x8-5mm-400-200-703-CM32
Probe	Neuronexus	A1x32-6mm-50-703-CM32